Flow pathways in multiple-direction fold hinges: Implications for fractured and karstified carbonate reservoirs

Published Version:
Flow pathways in multiple-direction fold hinges: Implications for fractured and karstified carbonate reservoirs / Pontes, Cayo C.C.; Bezerra, Francisco H.R.; Bertotti, Giovanni; La Bruna, Vincenzo; Audra, Philippe; De Waele, Jo; Auler, Augusto S.; Balsamo, Fabrizio; De Hoop, Stephan; Pisani, Luca. - In: JOURNAL OF STRUCTURAL GEOLOGY. - ISSN 0191-8141. - STAMPA. - 146:(2021), pp. 104324.1-104324.19. [10.1016/j.jsg.2021.104324]

Availability:
This version is available at: https://hdl.handle.net/11585/817625 since: 2021-03-31

Published:
DOI: http://doi.org/10.1016/j.jsg.2021.104324

Pontes, Cayo C.C.; Bezerra, Francisco H.R.; Bertotti, Giovanni; La Bruna, Vincenzo; Audra, Philippe; De Waele, Jo; Auler, Augusto S.; Balsamo, Fabrizio; De Hoop, Stephan; Pisani, Luca: *Flow pathways in multiple-direction fold hinges: Implications for fractured and karstified carbonate reservoirs*

JOURNAL OF STRUCTURAL GEOLOGY
VOL. 146
ISSN 0191-8141

DOI: 10.1016/j.jsg.2021.104324

Flow pathways in multiple-direction fold hinges: Implications for fractured and karstified carbonate reservoirs

Cayo C. C. PONTES[1*], Francisco H. R. BEZERRA[1], Giovanni BERTOTTI[2], Vincenzo LA BRUNA[1], Philippe AUDRA[3], Jo DE WAELE[4], Augusto S. AULER[5], Fabrizio BALSAMO[6], Stephan DE HOOP[2], Luca PISANI[4].

1 Dept. of Geology, Federal University of Rio Grande do Norte, Natal, Brazil

2 Dept. of Geoscience and Engineering, Delft University of Technology, Delft, The Netherlands

3 Polytech'Lab EA 7498, University Côte d'Azur, France

4 Bologna University, Department of Biological, Geological and Environmental Sciences, Via Zamboni 67, 40126 Bologna, Italy

5 Instituto do Carste, Carste Ciência e Meio Ambiente, Belo Horizonte, Brazil

6 NEXT - Natural and Experimental Tectonic Research Group, Department of Chemistry, Life Sciences and Environmental Sustainability, University of Parma, Italy

Abstract

Caves developed in carbonate units have a significant role in fluid flow, but most of these subsurface voids are below seismic resolution. We concentrated our study on four caves to determine the roles of fractures and folds in the development of karst conduits that may form flow pathways in carbonate reservoirs. We performed structural field investigations, petrographic analyses, and geometric characterization using Light Detection and Ranging (LIDAR) for caves in Neoproterozoic carbonates of the Salitre Formation, central part of the São Francisco Craton, Brazil. We found that the conduit shape, usually with an ellipsoidal cross-section, is a reflection of the tectonic features and textural variations. Carbonate layers containing pyrite and low contents of detritic minerals are generally karstified and appear to act as favorable flow pathways. Our results indicate that the development of the karst system is related to fracture corridors formed along parallel and orthogonal sets of fold hinges, which provide preferential pathways for fluid flow and contribute to the development of super-K zones. This study provides insights about the prediction of subseismic-scale voids in subsurface carbonate reservoirs, with direct application for the hydrocarbon and hydrogeology communities.

Keywords: Fracture corridors; Hypogene karst conduits; Salitre formation; Carbonate reservoir.

1. Introduction

Fractured and karstified carbonate rocks form significant hydrocarbon and groundwater reservoirs (Xu et al., 2017). Karst systems are formed where the dissolution of these rocks by the aqueous fluid is the dominant process (De Waele et al., 2009). Karst features are mainly controlled by structural heterogeneities such as bedding planes, faults and fractures, which affect fluid flow by providing preferential pathways for geofluids with the development of secondary porosity (e.g., Balsamo et al., 2016; Ennes-Silva et al., 2016, and references therein). This may influence the production and exploitation of oil reservoirs (Ogata et al., 2012; Frumkin, 2013; Klimchouk et al., 2017).

An accurate characterization of karst systems, common in carbonate reservoirs, requires special attention given that this type of reservoir represents 60% of the world's oil and 40% of the world's gas reserves (Montaron, 2008) and 25% of the water supply, up to 50% or more in some countries (Ford and Williams 2007). Therefore, they have high economic and social importance. Understanding the time-space evolution, geometry and size of karst porosity is fundamental in modeling and predicting fluid flow in carbonate aquifers and oil reservoirs (Popov et al., 2007; Agar and Geiger, 2015; Gholpoiur et al., 2016; Xu et al., 2017; Lyu et al., 2020).

The main mechanisms controlling karst distribution are chemical processes (oxidation of sulfides, and/or hypogenic biogenic CO_2), hydrothermalism, regional flow and regional and local structural control (Auler and Smart, 2003; De Waele et al., 2009; Ennes-Silva et al., 2016). Dissolution of carbonate rocks can occur by fluids enriched in CO_2 coming from the surface (epigenic karst, e.g., Audra and Palmer, 2011) or when ascending flow brings thermal CO_2-rich water (Dublyansky, 2012) or sulfidic fluids (Palmer and Hill, 2019). Fluids can also acquire their dissolutional aggressivity by mixing processes (for example, in coastal areas, Mylroie, 2012), or by localized oxidation of sulfides (e.g., pyrite) (Auler and Smart, 2003; Tisato et al., 2012a).

Folds may concentrate the highest strain in the fold hinge zone (Cosgrove, 2015), where fractures and fracture corridors occur. The term fracture corridor will be used to describe persistent subparallel fractures with consistent continuity (Ogata et al., 2014). These fractures often directly influence the fluid flow in the reservoirs and aquifers (Odling et al., 1999; Bagni et al., 2020).

The presence of karstified zones can cause problems such as loss of fluid circulation and well collapse in the exploited oil field (Xu et al., 2017). Therefore, decisions about reservoir prospecting and exploration are carried out amid many uncertainties arising from a poor understanding of the properties of these systems (Ogata et al., 2014; Klimchouk et al., 2016).

However, karst can also significantly enhance fluid flow in carbonate reservoirs (Pantou, 2014). Karst flow pathways may form very high-permeability zones (super-K zones), characterizing an important factor assessed in oil reservoirs (Questiaux et al., 2010; Ogata et al., 2012, 2014), which can connect different mechanical units and compartmentalize reservoirs in different stratigraphic levels (Questiaux et al., 2010; Bagni et al., 2020) and therefore optimize the oil production.

Even with the recent advances in knowledge about karst and fractures connecting different parts of rock masses (Pollard and Aydin, 1988; Matthäi and Belayneh, 2004; Narasimhan, 2005), several parameters such as karst evolution, geometry, structural control, and their influence on carbonate reservoirs have not been fully clarified through conventional exploration techniques such as seismic surveys because they are too small to be detected by seismic surveys or wells.

Major karst features can be observed at the seismic scale but, due to the limitation of the seismic resolution (>10 m), minor features often remain undetected (Tian et al., 2017). Several geoscientists have been applying new methodologies combined with seismic data to optimize the prediction of karst, such as thin section analyses and C/O isotope ratios of core samples, borehole images, 3D delineation methods (Tian et al., 2015 and references therein), and well-seismic inversion (Zhao et al., 2015).

However, despite the appreciable progress, major karst flowpaths are still often overlooked in conventional seismic lines.

Hence, the use of carbonate outcrop analogues (Guerriero et al., 2010, 2011; Santos et al., 2015; Giuffrida et al., 2019; La Bruna et al., 2018, 2020; Balsamo et al., 2020) could provide insights about these systems to minimize errors in development and production in carbonate reservoirs and allow for more reliable reservoir or aquifer reconstruction. To fill the aforementioned gaps, analogue outcrop studies can be used in some cases to supply the additional data required for the inter-well fracture property population (de Joussineau and Aydin, 2007; Panza et al., 2015).

This contribution focuses on the reconstruction of paleo-flow pathways below seismic resolution (less than 10 m) by analyzing subseismic-scale fractures and folds in four hypogenic karst systems developed within the carbonate succession of the Salitre Formation, (Fig. 1 a, b), an analogue of fractured and karstified reservoirs within the São Francisco Craton (SFC, Almeida et al., 2000) and adjacent areas.

In this study, we employed a multiscale and multidisciplinary approach involving petrographic characterization, qualitative and quantitative structural analysis, and high-resolution Light Detection and Ranging (LiDAR) imagery. LiDAR analysis was performed to provide first-order predictions on the occurrence and geometry of karst features and to better understand the relationship between diffuse or localized deformation on the development of flow pathways. We present a first-order prediction of the occurrence and geometrical attributes in karstified carbonate rocks to shed new light on the role played by both diffuse and localized deformation on the development of flow pathways.

'Figure 1 here'

2. Geological and speleological settings

The SFC (Almeida et al., 2000) (Fig. 1 a) corresponds to the western portion of a large cratonic area together with the Congo Craton in Africa, which were segmented during the Pangea breakup and opening of the South Atlantic Ocean in the Late Jurassic and Early Cretaceous (Alkmim and Martins-Neto, 2012; Cazarin et al., 2019). The most recent part of the SFC is composed of Meso- and Neoproterozoic sedimentary units: the Una Group, which overlaps both Paleoproterozoic and Archean basement units. Within the SFC, the Irecê and Una-Utinga basins were formed by rifting that occurred during the fragmentation of the Rodinia supercontinent (c. 950 – 600 Ma) (Condie, 2002; Guimarães et al., 2011). The presence of normal faults in the Una Group indicates that the extensional tectonic regime continued until the sedimentation of these Neoproterozoic basins (Misi and Veizer, 1998; Guimarães et al., 2011). A later deformation stage occurred during the Brasiliano orogeny (~ 650 – 500 Ma) (Misi and Veizer, 1998). Two main phases of deformation, marked respectively by folds and thrusts that strike NNE-SSW and E-W, are related to collisional events on the margin of the SFC during the Brasiliano orogeny (Guimarães et al., 2011; Ennes-Silva et al., 2016; Boersma et al., 2019).

The Salitre Formation represents an excellent natural laboratory to investigate the relationship between karst systems and fractured carbonate reservoirs. This unit occurs at the top of the Una Group, is approximately 500-m thick, and is mostly composed of carbonate units (Misi and Veizer, 1998). The Salitre Formation hosts hundreds of caves, including the longest cave systems in South America, with a combined length of over 140 km of passages (Auler et al., 2017). Most caves were developed in deep-seated confined conditions, formed by a combination of rising flow that migrated upward through the basal units and then spread laterally (Klimchouk et al., 2016) and oxidation of sulfide-rich beds in shallow aquifers (Auler and Smart, 2003). Bertotti et al. (2020) highlighted the local development of caves formed along strike-slip faults, displaying clear evidence of the interaction between silica-rich fluids and carbonate rocks during cave formation that is rarely observed in other settings worldwide.

In almost all cave systems, folds and related fractures control the planimetric development of the passages (Auler and Smart, 2003). The development of a huge number of caves in the Salitre Formation mostly occurred along fold hinges (Ennes-Silva et al., 2016; Boersma et al., 2019). The deformation features visible in the caves include stylolites, open mode fractures (joints and veins), stratabound (SB, confined within mechanical unit) and non strata-bound (NSB, smaller and greater than the mechanical unit) fractures and conjugate shear fractures (Ennes-Silva et al., 2016; Boersma et al., 2019, Balsamo, et al., 2020).

The stratigraphic features of the caves in the northern part of the Irecê basin were described by Cazarin et al. (2019). They identified five units from the bottom to the top: (1) grainstones with cross-bedded stratification, (2) fine grainstones with chert nodules, (3) microbial carbonates, (4) fine siliciclastic layers and marls, and (5) crystalline grainstone interfingered with chert layers. The compositional difference in these units is related to the variable degrees of diagenesis and provides these rocks different petrophysical properties. Some units concentrate fluid flow whereas others act as sealing units, preventing the fluid flow and intensifying the dissolution in the underlying layers (Cazarin et al., 2019; Balsamo et al., 2020).

3. Methods

In this study, four caves were selected, known by local name: the Ioiô, Torrinha, Lapinha, and Paixão (Fig. 1b). All caves are interpreted as displaying features associated with confined flow/hypogenic conditions (Auler, 1999), although epigenic features (and earlier) may occur. Data integration allowed for clarifying the relationship between the physical properties of the host rocks and both fracturing and karstification processes. We describe the above-mentioned analyses in the following sections.

3.1 Petrographic and lithostratigraphic analyses

The laboratory work included the petrographic analysis of 22 thin oriented sections obtained from samples collected in the caves. The petrographic analysis was carried out using a Leica DMLP optical microscope under planar and cross-polarized lights. Based on their texture, carbonate rocks were described according to Dunham (1962). This analysis allowed for us to define the composition, sedimentary facies, and texture of the karstified carbonates. Four stratigraphic columns, one for each cave, were reconstructed and sampled in key sectors. This approach was employed to understand which units had the highest degree of dissolution (more dissolved) based on the distribution of facies and mineral composition.

3.2 Structural analysis

Deformation features in the caves of the Salitre Formation were measured and sorted into different types: mode I fractures (joints and veins), bed-parallel stylolites, conjugate shear fractures (i.e, minor faults), and fold hinges. Joints and veins include both SB and NSB structures. Bedding attitude and dip variations were also measured systematically. Detailed qualitative and quantitative structural analyses were carried out at each site studied. The qualitative analysis aimed at deciphering the nature, kinematics, relative timing, and attitude of individual features affecting the carbonate rock multilayers.

Moreover scanline analyses were performed (Marrett et al., 1999; Ortega et al., 2006; Miranda et al., 2014; Giuffrida et al., 2019; Pontes et al., 2019). In total, 603 fractures were measured, interpreted and analyzed with stereonet software (Allmendinger et al., 2011). These analyses were performed along the sub-vertical walls at the external portion of cave entrances. At each site analyzed, the 5-m-long parallel-to-bedding scanlines were located orthogonally to the main fracture striking-sets (N-S and E-W direction) to be as representative as possible of all the structural features present. For each fracture, we measured the following parameters: attitude, height, distance from the origin of the scanline, type (joint, shear joint, fault), aperture and infill (if present). The aperture was measured using a comparator developed by Ortega et al. (2006). The real spacing between fractures was calculated with trigonometric equations using the azimuthal angle formed by the scanline plunge/dip and the main strike/dip of each set (Terzaghi, 1965). The Coefficient of variation (Cv) was calculated; it consists of the ratio between the $\sigma 1$ standard deviation and the mean value of fracture spacing of individual fracture sets (Zambrano et al., 2016; Giuffrida et al., 2019). Furthermore, the best-fit equations were calculated for the recognized individual fracture striking-sets.

This distinction among fracture striking-sets was determined by plotting the mean fracture spacing and their cumulative number, cn, in bi-logarithmic plots (Gillespie et al., 1993; Railsback, 1998; Odonne et al., 2007).

3.3 LiDAR survey

The caving club “*Grupo Bambui de Pesquisas Espeológicas*” provided the cave maps with topographic data from the caves. Using these maps, it was possible to formulate data acquisition strategies for LiDAR, boundary outlines, and the structural maps of caves. The purpose of this technique was to understand the karst geometry and the relation with the fracture pattern. We carried out scanning with a terrestrial LiDAR system (TLS) using a Leica Scanstation P40 scanner from ViGeA (Reggio Emilia, Italy) and a mobile LiDAR system (MLS), a ZEB-Revo GeoSLAM scanner. The MLS shows better results for the cave morphology and irregularities in the passages. In addition, the user could go through complex cave passages with the MLS during the acquisition of the 3D point clouds without changing stations, which provided quick and better results to identify the cave morphology. The TLS can provide more accuracy and precision due to the series of additional sensors such as an inclinometer, an electronic compass and a dual-axis compensator (Fabbri et al., 2017; De Waele et al., 2018) LiDAR scanning can reveal the importance of fractures in karstification (Jacquemyn et al., 2012). At least 35 M points were acquired for each cave studied.

We processed the point clouds with the open-source software Cloud Compare using the raw file from the LIDAR data. Cloud Compare offers several tools to improve the analysis of cave morphology (Fabbri et al., 2017; De Waele et al., 2018) and geometry. MLS data were loaded to plot the intensity values of the scalar field using grayscale.

For a good visualization of the structural features, we used the “Eye-dome Lighting” filter. We created 3D model slices of several parts to visualize the geometry around and inside the cave using the “Cross Section” tool. Approximately 1.4 km of cave passages were surveyed, approximately 350 m in the Ioiô cave, 500 m in the Torrinha cave, 240 m in the Lapinha cave, and 200 m in the Paixão cave.

4. Results

4.1 Lithostratigraphy of cave systems

In the area of the four investigated caves, the carbonate rocks of the Salitre Formation are arranged in millimeter- to centimeter-thick tabular layers. Stratigraphic analysis indicates three main lithologies, from the base to the top: (a) microbial carbonates, (b) microbial carbonates with intercalations of siltstone levels, and (c) sedimentary breccia (Fig. 2a).

'Figure 2 here'

The carbonate layers that are microbial carbonate display chert nodules or dark *boudin* concretions in some portions (Fig. 2a.). The thin sections analysis indicates that the texture of these carbonate layers are mudstones affected by an intensive process of dolomitization. The primary porosity of lithologies that compose the Salitre Formation was reduced mostly by mesodiagenesis cementation (Cazarin et al., 2019). The secondary porosity was mostly represented by fractures. The mudstone interval shows a smaller grain size, with a particle-size distribution classified as silt, with frequent chert nodules and pyrite present (Fig. 2 b, c).

The microbial carbonate with siltstone levels is a mudstone (Fig. 2 d, e) affected by dolomitization and characterized by detritic minerals that correspond to 10-20% of their composition. The sedimentary breccia (Fig. 2 f, g) corresponds to grainstone characterized by a coarse grain size (sands). Specific layers display less significant dissolution compared with others, forming high relief zones (prominent layers) that vary according to rock texture and composition (Fig. 3). Usually, the mudstone with siltstone levels and the grainstone are more prominent in relief inside the caves than the mudstone layers (Fig. 3). Occasionally within the mudstone layers, we identified darker intercalations composed of organic material and/or pyrite (Fig. 2 c), which indicate a reducing environment.

'Figure 3 here'

4.2 Structural data

We divided this topic into quantitative and qualitative approaches. The qualitative approach included detailed structural mapping and LiDAR imaging analysis to identify the relationship between the fracture sets and principal fracture zones, as well as the characterization of the cave features. A quantitative field fracture analysis was performed along the surveyed carbonate rock walls to distinguish the diffuse deformation from the fold-fault related deformation and determine their influence on the cave's nucleation and development.

4.2.1 General cave features

The qualitative structural analysis based on field observations, LiDAR imaging, and structural measurements was performed within the caves and along the external sub-vertical walls that surround the cave entrances. We documented fractures (joints, veins, sheared joints, and sheared veins), bed-parallel stylolites, sedimentary bedding, and fold hinges. Commonly, bed-parallel stylolites are located at the bed interfaces within mm-thick, continuous, clay-rich marl levels. Less often, they are present within individual carbonate beds. Open-mode fractures may display hackles and ribs and thus were identified as joints. In some cases, a millimeter-to-centimeter offset of depositional surfaces was observed across them and thus we considered the above features to be sheared joints. Some of the cave passages exhibit an alignment of speleothems located in the central part of the cave roofs. These speleothems are mainly associated with several fracture zones parallel to the cave passages and running along the central part of the cave roofs (Fig. 4 a). The cave passages are arranged in a linear or maze pattern, with rectilinear sub-horizontal passages developed parallel to fractures in an orthogonal pattern (Fig. 4 a, b). High dissolution zones occur in the middle portion of the cave passages (Fig. 4 c). In general, cave galleries could be divided into major chambers ~ 10-m high and smaller conduits up to 2.5-m high that link the major chambers. The preferred direction of the cave passages coincides with the main persistent N-S- and E-W-striking fracture zones.

'Figure 4 here'

Fractures may be confined within individual carbonate beds as SB, usually observed away from the main dissolution zones, or as NSB where they crosscut one or several beds, usually related to main dissolution zones. Both SB and NSB fractures are much more evident along the external portion of the caves where the dissolution and mineralization processes do not entirely erase or overprint them (Fig. 5 a, b). The SB and NSB fractures are not necessarily parallel (Fig. 5 c). However, the high dissolution zones are parallel to the main persistent NSB fractures.

'Figure 5 here'

Two main fracture sets were observed in the study sites, striking N-S and E-W; systematically, the E-W fractures terminate against the N-S ones, which indicates that the latter are older than the former (Fig. 6 a). Bed-parallel stylolites are common throughout the analyzed sites, at the surface and inside the caves. We also documented bed-perpendicular folded veins (Fig. 6 b) and several high-angle normal faults characterized by extensional or oblique kinematics (Fig. 6 c and d). Usually, these structures are composed of several discontinuous slip surfaces; the abutting/crosscutting relationships (Fig. 6 d) among the fracture sets are consistent with their hierarchical formation and subsequent shearing of joint sets sub-parallel to the main slip surfaces (Davatzes and Aydin, 2003; Myers and Aydin, 2004).

'Figure 6 here'

4.2.2 Identification of fold hinges and fracture sets

Two major gentle folds occur in the Ioiô cave (Fig. 7 a, b, c, d). These antiforms display a N-S fold axis, which is parallel to the main cave passage and the main fracture/dissolution zones (Fig. 7 e, f). Along the cave passages, the bed surfaces display a dip of approximately 10º toward the west (along the western cave wall) and 10º toward the east (along the eastern wall, Fig. 7 c, d, g).

'Figure 7 here'

We performed LiDAR surveys in all the caves. In the Lapinha cave (Fig. 8 a) the LiDAR survey was integrated with detailed structural analysis at 13 sites (Fig. 8 b). This cave is marked by the presence of two orthogonal, bed-perpendicular fracture sets that strike ~ N-S and E-W (Fig. 8 c). Along the ~ N-S passages, the bed surfaces show dip ranging from 3º to 15º toward the east and west. E-W cave passages show a bedding dip from 5º to 10º toward the north and south (Fig. 8 d and e). The main fracture/dissolution zones are parallel to the documented fold hinges and concentrated along the central portion of the cave ceilings (Fig. 8 c, d). Furthermore, the LIDAR data analysis allowed for us to highlight and measure the fold wavelengths in the Lapinha cave. E-W and N-S folds display an almost equidistant wavelength of ca 30 m (Fig. 8 e).

'Figure 8 here'

The high-resolution imaging provided by the MLS survey in a maze portion of the Torrinha cave provides a consistent representative model of the geometry of the cave passage (Fig. 9 a, b) and allowed for us to determine that the karstification processes followed the direction of fold hinges. The main geometric pattern observed for the cave passages could be associated with an ellipsoid with a major axis in a horizontal or vertical position (Figs. 9 b, c, d). The processes of dissolution are more developed near or at the fracture/fault intersection, as highlighted in the 3D model of the Paixão cave (Fig. 9 e) and Fig. 4 b.

'Figure 9 here'

The studied mazes in Torrinha cave displays a similar structure to the Lapinha cave, characterized by an orthogonal pattern of the cave passages. This geometry is highlighted by the LiDAR survey carried out in the southeastern part of the cave (Fig. 10 a). Along this portion, the cave is affected by folds showing both N-S and E-W hinge directions (Fig. 10 b, c). The bedding dip ranges from 8º to 15º, usually in opposite directions, forming gentle folds (Fig. 10 c, d). The E-W passages usually terminate against the N-S structures, which are more persistent. A NW-SE strike-slip fault with a dextral kinematic (Fig. 10 c) causing a displacement of N-S fold hinges was observed. The detachment of carbonate layers indicates a compressive component (Fig. 10 e).

'Figure 10 here'

The Paixão cave is characterized by orthogonal cave passages and related anticlines (Fig. 11 a) where these passages display an *en echelon* pattern associated with several *en echelon* fold hinges (Fig. 11 b, c). The bedding dip ranges from 4º to 18º along the cave walls (Fig. 11d). One of the main cave passages is associated with a single fault zone (Fig. 11 e) showing high displacement (HD) in the central part, observed in the LiDAR digital model (Fig. 11 g). Along this fault zone, we also identified and characterized several dip-slip faults (Figs. 11 g, h).

'Figure 11 here'

4.2.3 Background and clustered fractures

The quantitative structural analysis based on the scanline methodology was performed along the external vertical walls. The scanline measurements were taken to decipher the nature, orientation, geometry, dimension, and multi-scale properties of background and clustered fractures. The values of the exponential distribution, power law distribution and Cv are summarized in table 1.

'Table 1 here'

The N-S-striking set shows Cv values higher than 1 for the Ioiô (Fig. 12 a), Lapinha (Fig. 13 a), and Torrinha sites (Fig. 14 a), and values lower than 1 for the Paixão site (Table 1). The same results were observed for the NNW-SSE-striking set. The Cv values of the NW-SE-striking set are close to 2 in the Ioiô site; they range from 0.8 and 1.7 in the Torrinha site and they from 0.29 to 0.99 in the Paixão site. In the Ioio site, the E-W- and NE-SW-striking sets show Cv values lower than 1. However, in the Torrinha and Lapinha sites, which exhibit caves with maze geometries, the E-W- and NE-SW-striking sets exhibit Cv values higher than 1, reaching 2.26 at scanline 1 of the set NE-SW (Table 1). Only in the Paixão site, all striking-sets (Fig. 15 a) present Cv values lower than 1 for all scanlines.

'Figure 12 here'

'Figure 13 here'

The multi-scale spacing distribution computed for the SB and NSB fracture sets (Figs. 12 b, 13 b, 14 b, 15 a) is presented in Figures 12 c, 13 c, 14 c, and 15 b, in which the fracture spacing is plotted in a log-log space versus as a cumulative number. In the Ioiô site, the N-S-striking set (Fig. 12 b, 13 b, 14 b, 15 a) shows a power-law distribution (Fig. 12 c); the same occurs at scanline 3 in the Torrinha site (Fig. 14 c). All other N-S striking-set scanlines show an exponential distribution in the Lapinha and Paixão sites

(Figs. 13 c, 15 b). The NNW-SSE- and NW-SE-striking sets present the same behavior as the N-S-striking set. In the Ioiô and Torrinha sites, the E-W-striking set shows an exponential distribution. In the Lapinha site, the E-W-striking set presents both an exponential and power-law distribution (Fig. 13 c). In the Paixão cave, all measured striking-sets, N-S, NW-SE, and NNW-SSE, exhibit an exponential distribution (Fig. 15 b). The NE-SW-striking set in the Ioiô and Lapinha sites show a power-law distribution (table 1). In all cave sites, the clustered fracture sets (fracture corridors) exhibit the same trend as that in the main cave passage.

'Figure 14 here'

'Figure 15 here'

5. Discussion

5.1 The origin and evolution of fracture corridors and flow pathways in multiple-direction fold hinges

The prediction of flow pathways that connect different parts of reservoirs may provide useful information to interpret fluid flow at a subseismic scale and could optimize oil field development planning. The evolution of subseismic flow pathways in multiple-direction fold hinges may be explained in four stages: background deformation, E-W compression, N-S compression, and karst development. Quantitative analysis performed for our study sites allowed for discriminating the fracture sets associated with a previous stress field related to burial (background deformation) from the fracture sets related to the fold-fault events that could play a key role in fluid migration processes.

Focusing on the fractures that have been analyzed, the first stage (background deformation) is characterized by cross-orthogonal bed perpendicular joints related to diffuse deformation in different striking sets. Fracture sets related to diffuse deformation and the bed-parallel stylolites could be associated with the overburden of the Salitre Formation (Figure 16 a, Ennes Silva et al., 2016). The bed-parallel stylolites occur inside the stratigraphic layers as well as in the interface between layers. The burial deformation is the first stage marked by the aforementioned fracture sets and bed-parallel stylolites. Permutation of the sub-horizontal σ_2 and σ_3 principal stress likely took place during burial diagenesis of the studied carbonate succession allowing for the formation of both N-S and E-W fracture sets (Bai et al., 2002). The joint sets are mainly characterized by a negative exponential, multi-scale spacing distribution, which is distinctive of a diffuse deformation (Ortega et al., 2006). Moreover, the range of Cv variations is consistent with randomly distributed fractures (Gillespie et al., 1993).

The second stage of evolution of flow pathways is related to E-W compression (Fig. 16 b). This tectonic compression occurred during the major folding event, N-S shortening, related to the Brasiliano orogeny (Ennes Silva et al., 2016), which developed gentle fold sets that display fold hinges mainly striking N-S (Fig. 7 d, e). During this second stage of deformation, nucleation and development of the NW-SE, NE-SW, NNE-SSW and NNW-SSE-striking fracture sets occurred. These structural elements were associated with the shearing of the pre-existing N-S fractures and the development of incipient faults (Figs. 6 c, 6 d, 11 e, 11 f, 11 g, 11 h). These fracture sets were described by a power-law distribution, typical of clustered deformation. Cv values usually range from 1.03 to 2.2 and thus these fracture sets are ascribed to a folding event or a mature stage of faulting (de Joussineau and Aydin, 2007).

The third stage is the development of folds displaying a basin-dome configuration (Ramsay, 1967) due to N-S shortening (Fig. 16 c). E-W fold hinges and NW-SE strike-slip faults (Fig. 10 c, e) characterize this tectonic compression. A displacement of the N-S fold hinge reinforces that the N-S trends predate the development of this strike-slip fault. These two contractional phases were also documented by previous research conducted by Cruz and Alkmim (2006), Guimarães et al. (2011), Ennes-Silva et al. 2016, Klimchouk et al. (2016), D'Angelo et al. (2019) and Balsamo et al. (2020). Ennes-Silva et al. (2016) proposed the generation of a superposed fold pattern initiated by NW-SE-oriented compression, which initially formed NNE-SSW-oriented joints and E-W folds and then E-W-oriented joints and N-S folds associated with a thrust in the northern portion of the Salitre Formation. In our study in the southern portion of the Salitre Formation, we suggest that the first contractional phase is evidenced by E-W compression that originated N-S and NNE-SSW fold hinges and N-S-striking fractures that are more pervasive than the E-W fold hinges and E-W-striking fractures. This sequence of contractional events, with E-W structures younger than N-S, was also documented by D'Angelo et al. (2019). E-W-oriented fractures abut against N-S-striking fractures, supporting this interpretation.

In the proposed generation of superposed folds, the development of fracture corridors predates the entry of fluid into the system, which represents the last stage on the development of flow pathways. The same brittle mechanism with contractional control was documented by Agosta and Aydin (2006), La Bruna et al., (2017), and Mazzoli et al. (2014) for tight carbonates cropping out in central and southern Italy, which were interpreted as a poly-phasic tectonic activity. From the cross-cutting and abutting relationship, it is possible to deduce that the E-W-striking fractures developed later than the N-S-striking fractures (Fig. 6 a; 10 c), Moreover, along the intersection or fracture termination zones, the karstification process is enhanced (Fig 4 b, 9 d). Bed-parallel stylolites and bed-perpendicular folded veins indicate the variation in the stress fields that affected these carbonate rocks (Fig. 6 b). Based on the crosscutting relationship, it is possible to deduce that the bed-parallel stylolites predate bed-perpendicular folded veins.

After the development of both fracture sets and the extension localized along fold hinges, rising fluid flow interacted with the surrounding rocks (Figure 16 d). Due to the very low primary porosity of the carbonate rocks, ranging from 0% to 7% (Cazarin et al., 2019), the fractures acted as preferential fluid pathways. NSB fracture corridors localized along fold hinges increased permeability and connectivity (Fig. 3, 4 a, 4 b) (Bagni et al., 2020). The fluid-rock interaction may directly affect the fluid flow and storage (Evans and Fischer, 2012), making high dissolution zones (super-K zones) (Figs. 4 c, 7 e, 7 f). The high dissolution/karstification rate following fracture corridors is evidenced by the cave pattern, forming a typical hypogene maze, and the lack of the downward carving vadose infiltration passages typical of epigenic cave systems. The alignment of speleothems following these fractures highlights the presence of the structural fluid flow pathways, which are still exploited by present epigenic infiltrating waters (Fig. 3, 4 a, Kim and Sanderson, 2010).

The fourth stage of development of karst conduits is related to lithologic/stratigraphic control. Even with the development of cave passages along fold hinges, differential degrees of karstification (Fig. 3) in the observed lithologies, based on the cross-section morphology of the cave, indicate that the development of the karst in carbonate rocks is also related to their composition. Field and laboratory analyses suggest that the composition of these rocks definitely influenced can influence the karst development (de Melo et al., 2015; Baiyegunhi et al., 2017). Carbonate rocks that have a finer grain size are more readily dissolved (Fig. 2 c), which would have focused the dissolution process and the fluid flow. Moreover, the presence of pyrite (Worthington and Ford, 1995; Palmer, 2016) (Fig. 2 c) may have contributed to an increase in the karstification process by H_2S oxidation (Auler and Smart, 2003; Tisato et al., 2012; D'Angeli et al., 2019). The primary porosity of these rocks is very low, so it is the secondary porosity (i.e., fractures, that are strongly related to the rock composition, Balsamo et al., 2020) that guides karstification (Cazarin et al., 2019). The layers characterized by lower dissolution rates correspond to grainstone with clasts and a coarser grain size (Fig. 2 f, g) and mudstone interspersed with siltstone levels with high detritic mineral content (15-20%), mainly quartz grains (Fig. 2 d, e). The compositional variation in the wall rocks leads to the present-day visible karst geometry.

'Figure 16 here'

5.2 Development of karst conduits according to the deformation stages

The development of karst conduits in the Salitre Formation's carbonate units follows the structural and compositional controls mentioned above, but each cave has unique characteristics. We performed a statistical analysis to provide a useful model for comparison of the fracture sets that influenced the development of karst conduits in each cave. For the Ioiô cave (Fig. 7), the N-S-, NW-SE-, and NE-SW-striking sets show a power-law distribution rather than an exponential distribution, and they could be associated with a localized deformation (fold-fault related, Ortega et al., 2006). The Cv of these fracture sets is higher than 1 whereas the N-S sets display Cv values greater than 1.9. Therefore, we affirm that the N-S-, NW-SE-, and NE-SW-striking sets are clustered, and could be related to a folding process. The E-W-striking fracture set displays an exponential distribution and lower Cv of 0.85 and 0.75, which indicate a diffuse deformation. As the N-S-, NW-SE-, NNW-SSE-, and NE-SW-striking sets show a power-law distribution in the Ioio site (Table 1), we conclude that the development of the Ioiô cave passages is related to fold-related fractures concentrated along fold hinges.

In the Lapinha cave (Fig. 8), all fracture sets (NE-SW, N-S, WNW-ESE, and E-W) show Cv values greater than 1, which indicates a clustered deformation (Gillespie et al., 1993; de Joussineau and Aydin, 2007). Only the NE-SW-striking set, with a Cv value of 2.26, shows a power-law distribution (Table 1). The range of Cv variations is consistent with both even-spaced and clustered fracture distributions in the carbonates (Gillespie et al., 1993), The Cv higher than 1 and variation in the power-law and exponential distributions implies that multiple-stage jointing occurred during the burial and subsequent evolution of the Salitre Formation.

The striking sets of the Torrinha cave (N-S, NNW-SSE, NW-SE and E-W, Fig. 10 b) show a similar behavior, with Cv values higher than 1, but only the N-S striking set shows more power-law distribution than exponential distribution, which is related to the aforementioned multiple-stage jointing. We suggest that mostly N-S-oriented joints were formed during the fold event, and NNW-SSE-, NW-SE- and E-W-oriented striking sets may be formed during the burial and may have reactivated during a tangential stress regime.

In the Paixão cave (Fig. 11 a), the N-S-, NW-SE- and NNW-SSE-striking sets (Figure 15 a) show a better correlation with the exponential distribution than a power-law distribution. The Cv of these sets is lower than 1, from 0.34 to 0.88. Based on these values and the good correlation with an exponential distribution, we suggest that these fractures do not originate during the folding process. These striking sets may have formed during the burial history of the Salitre Formation, and may have reactivated during the folding event.

Faults may form preferential flow paths and guide fluid migration (Ligtenberg, 2004; Wilson et al., 2011; Ogata et al., 2012, 2014; Balsamo et al. 2019). Karst development may also follow fracture corridors generated in fault damage zones (Fig. 10 e, Ogata et al., 2014). The process of karstification in faults as well as in folded zones is observed worldwide, for example, in the Tarim Basin where these areas represent ideal targets for oil (Xu et al., 2017). In the Paixão cave, it was observed that cave passages developed following an *en echelon* pattern (Fig. 10 b, c). In the central portion of the fault zone, which has the highest deformation and displacement rates (Ogata et al., 2014), a subvertical master fault was observed (Fig. 10 e, f) and a transtensive structure developed at the edge of the fault zone (Fig. 10 g, h). This allows for us to affirm that cave passages follow both anticline fold hinges and fault zones.

5.3 Implications for fluid flow in carbonate units

Tectonic structures greatly impact the fluid flow in carbonate units (Goldscheider, 2005; Dewever et al., 2010; Pantou, 2014; Agosta et al., 2015; Cosgrove, 2015; Ennes-Silva et al., 2016; Wang et al., 2017; Boersma et al., 2019; Balsamo et al., 2020). Structures such as fracture corridors often form preferential zones for fluid flow (Ogata et al., 2014; Souque et al., 2019), but the location of their occurrence is an enormous challenge for the oil industry because they are barely visible at a seismic resolution (Lamarche et al., 2018). Understanding the key factors in their formation, distribution and geometry may contribute to flow modeling for fractured carbonate rocks (Goldscheider, 2005) and to the assessment of their impacts on the development of karstified reservoirs.

Structural data allowed for correlating diffuse and localized fold-fault-related deformation with influence on the development of the hypogenic caves analyzed. This information provides new insights on storage and fluid flow properties. The qualitative analysis indicates that the development of the karst-conduits investigated is mainly related to highly persistent fractures, usually visible along the central portion of the roofs of these caves and parallel to the fold hinges (Evans and Fischer, 2012), creating a high-dissolution zone (Figures 4 c, 7 e, f). This evidence was also reported and documented in many other cases around the world, including the Middle East oil fields, pre-salt reservoirs offshore Brazil and the Tarim Basin in China (Pollastro, 2003; Menezes et al., 2016; Li et al., 2018). Li et al. (2018) highlighted that trending fractures in the extensional area of faulted folds are better developed than the fractures in the limb of folds improving the migration of fluids and permeability in tight sandstone reservoirs. Based on our observations of high-dissolution zones located in the extensional area of folds (Fig. 3; 7 c, d), it is possible to verify the same behavior in carbonate rocks and carbonate reservoirs.

Fluid flow events in carbonates subdued by tectonic compression was described by Warren et al. (2014), who integrated isotope data with structural surveys. Morley et al. (2014) highlighted the relevance of fluid flow along fold-thrust belts in deep aquifers and onshore (offshore Brunei and the Central Basin of Iran, respectively). Both works highlight the importance of fractures in the migration of fluids and in the fluid-rock interaction. Here, we highlight the importance of fracture corridors that, similar to fractures, act as fluid pathways in fold and thrust environments.

The use of LiDAR was demonstrated to be a very useful tool for detailed cave mapping. Fabbri et al. (2017b) used TLS to make detailed 3D models for morphometric measurements. De Waele et al. (2018) used TLS and 3D photogrammetry to identify different evolution stages of ceiling channels. Here, we applied both TLS and MLS to observe the karst geometry/shape (Fig. 3, 7 e, 11 f); the MLS showed more accurate results due to the ability to move the instrument through both narrow and large cave passages without interrupting during acquisition.

The karst conduit shape is a response to the interaction between structural features and the composition of the carbonate rocks. Structural features such as fractures and fracture corridors provide space for vertical rising flow, and horizontal enlargement occurs laterally along preferential carbonate layers (Klimchouk, 2009). This enlargement occurs manly in presence of mudstones with a silt grain size and pyrite content that boost the carbonate dissolution by sulfide oxidation. Carbonate layers with a coarse grain size and higher detritic mineral content that are absent of pyrite may hinder the fluid flow and concentrate the dissolution in subjacent layers, confining the ascending fluid and intensifying a horizontal fluid circulation (Klimchouk et al., 2016), leading to the ellipsoidal cross-sectional shape of the karst corridors.

Hence, the development of the hypogenic caves studied following the structural control (Ennes-Silva et al., 2016; Boersma et al., 2019) of the area, mainly expressed as fracture corridors along orthogonal fold hinges. These fracture sets were initially randomly distributed and reactivated during the folding event, with preferential N-S and E-W strikes, providing localized deformation in the fold hinges generated by the compression that affects the carbonate rocks (Ennes-Silva et al., 2016; Boersma et al., 2019; Balsamo et al., 2020). These structural elements result from the shearing and linkage of pre-existing, bed-confined N-S and E-W fractures and the formation of NW-SE-, NE-SW-, NNE-SSW-, and NNW-SSE-striking tail joints, which clustered at the mode-II extensional quadrants and along the Mode-III terminations of the sheared N-S and E-W elements (sensu Segall and Pollard, 1983; Peacock et al., 1997; Agosta et al., 2015).

The positions of fold-hinges control the fold-related N-S and E-W fractures (Awdal et al., 2016) and the development of fracture corridors and karst conduits. Although fracture corridors are barely visible on the subseismic scale (Lamarche et al., 2018), these tectonic structures could be related to regional structures, such as fold hinges, that could be observed on maximum-curvature maps (Fischer and Wilkerson, 2000), for example.

6. Conclusions

The structural data and the karstification processes that affect the carbonate rocks of the Salitre formation indicate that the caves develop following the main structural features of the area, which is strongly influenced by fold hinges and faults. The major results of this research contribute to the prediction of karst geometry and occurrence, and are summarized below:

(a) In plan view, the cave passages are orthogonal, with a maze pattern, following the structural control of the area, and are expressed as fracture corridors along fold hinges and faults. The development of subseismic flow pathways is directly related to the structural features that affect these rocks.

(b) The vertical profile of the cave passages shows an ellipsoidal shape/geometry due to the textural variation that provides different karstification levels. Carbonate layers that have more pyrite and less detrital minerals in their composition are more karstified and can act as flow pathways. Carbonate layers with a coarser grain size and higher detrital minerals content hinder the karstification. These layers often act as seals to rising fluid flow.

(c) Fracture corridors are formed along fold hinges, even in gentle folds with a bedding dip less than ~10º. These fracture corridors behave like high-permeability zones (super K-zones) that facilitate the vertical fluid percolation and the karstification process. These fracture corridors are strongly related to fluid migration.

(d) Cave passages may develop during or after faulting. The secondary porosity due to faulting is essential to fluid percolation. In addition, the karstification process is intensified at intersections between distinct fractures sets.

(e) The subseismic flow pathways and karst conduits can be predicted by the accurate structural analysis. Both diffuse and localized deformation, related to folds or faults, may increase the process of karstification. The development of subseismic flow pathways and karst conduits is intensified in a localized deformation due to the clustered fractures that provide pathways and enhance the fluid flow.

Acknowledgements

This research was carried out in association with the ongoing R&D project registered as ANP 20502-1, “Processos e Propriedades em Reservartórios Carbonáticos Fraturados e Carstificados – POROCARSTE 3D” (UFRN / UNB / UFRJ / UFC / Shell

Brasil / ANP) – Porokarst – Processes and Properties in Fractured and Karstified Carbonate Reservoirs, sponsored by Shell Brasil under the ANP R&D levy as “Compromisso de Investimento com Pesquisa e Desenvolvimento”. Cave maps were kindly provided by Grupo Bambuí de Pesquisas Espeleológicas. Cave sampling was performed through SISBIO permit 63178/1. Many thanks to Alisson Jordão and Uilson Teixeira for the fieldwork and Umberto Del Vecchio of ViGeA Reggio Emilia (Italy) for the fieldwork and elaboration of the TLS surveys.

References

Agar, S.M., Geiger, S., 2015. Fundamental controls on fluid flow in carbonates: Current workflows to emerging technologies. Geol. Soc. Spec. Publ. 406, 1–59. https://doi.org/10.1144/SP406.18

Agosta, F., Aydin, A., 2006. Architecture and deformation mechanism of a basin-bounding normal fault in Mesozoic platform carbonates, central Italy. J. Struct. Geol. 28, 1445–1467. https://doi.org/10.1016/j.jsg.2006.04.006

Agosta, F., Wilson, C., Aydin, A., 2015. The role of mechanical stratigraphy on normal fault growth across a Cretaceous carbonate multi-layer, central Texas (USA). Ital. J. Geosci. 134, 423–441. https://doi.org/10.3301/IJG.2014.20

Alkmim, F.F., Martins-Neto, M.A., 2012. Proterozoic first-order sedimentary sequences of the São Francisco craton, eastern Brazil. Mar. Pet. Geol. 33, 127–139. https://doi.org/10.1016/j.marpetgeo.2011.08.011

Allmendinger, R.W., Cardozo, N., Fisher, D.M., 2011. Structural geology algorithms: Vectors and tensors, Structural Geology Algorithms: Vectors and Tensors. https://doi.org/10.1017/CBO9780511920202

Almeida, F.F.M. De, Brito Neves, B.B. De, Dal Ré Carneiro, C., 2000. The origin and evolution of the South American platform. Earth Sci. Rev. 50, 77–111. https://doi.org/10.1016/S0012-8252(99)00072-0

Audra, P., Palmer, A.N., 2011. Structure des réseaux karstiques : Les contrôles de la spéléogenèse épigène. Geomorphol. Reli. Process. Environ. 359–378. https://doi.org/10.4000/geomorphologie.9571

Auler, A.S., 1999. Karst evolution and paleoclimate of eastern Brazil. University of Bristol.

Auler, A.S., Smart, P.L., 2003. The influence of bedrock-derived acidity in the development of surface and underground karst: Evidence from the Precambrian carbonates of semi-arid northeastern Brazil. Earth Surf. Process. Landforms 28, 157–168. https://doi.org/10.1002/esp.443

Auler, A.S., Klimchouk, A., Bezerra, F.H.R., Cazarin, C.L., Ennes-Silva, R., Balsamo, F., 2017. Origin and Evolution of Toca da Boa Vista and Toca da Barriguda Cave System in North-eastern Brazil, in: Hypogene Karst Regions and Caves of the World, Cave and Karst Systems of the World. pp. 827–840. https://doi.org/10.1007/978-3-319-53348-3_56

Awdal, A., Healy, D., Alsop, G.I., 2016. Fracture patterns and petrophysical properties of carbonates undergoing regional folding: A case study from Kurdistan, N Iraq. Mar. Pet. Geol. 71, 149–167. https://doi.org/10.1016/j.marpetgeo.2015.12.017

Bagni, F.L., Bezerra, F.H., Balsamo, F., Maia, R.P., Dall'Aglio, M., 2020. Karst dissolution along fracture corridors in an anticline hinge, Jandaíra Formation, Brazil: Implications for reservoir quality. Mar. Pet. Geol. 115, 104249. https://doi.org/10.1016/j.marpetgeo.2020.104249

Bai, T., Maerten, L., Gross, M.R., Aydin, A., 2002. Orthogonal cross joints: Do they imply a regional stress rotation? J. Struct. Geol. 24, 77–88. https://doi.org/10.1016/S0191-8141(01)00050-5

Baiyegunhi, C., Liu, K., Gwavava, O., 2017. Diagenesis and reservoir properties of the Permian Ecca Group sandstones and mudrocks in the Eastern Cape Province, South Africa. Minerals 7(6), 88. https://doi.org/10.3390/min7060088

Balsamo, F., Bezerra, F.H.R., Klimchouk, A.B., Cazarin, C.L., Auler, A.S., Nogueira, F.C., Pontes, C., 2020. Influence of fracture stratigraphy on hypogene cave development and fluid flow anisotropy in layered carbonates, NE Brazil. Mar. Pet. Geol. 114, 104207. https://doi.org/10.1016/j.marpetgeo.2019.104207

Balsamo, F., Clemenzi, L., Storti, F., Solum, J., Taberner, C., 2019. Tectonic control on vein attributes and deformation intensity in fault damage zones affecting Natih platform carbonates, Jabal Qusaybah, North Oman. Journal of Structural geology, v. 122, pp. 38-57. https://doi.org/10.1016/j.jsg.2019.02.009

Balsamo, F., Clemenzi, L., Storti, F., Mozafari, M., Solum, J., Swennen, R., Taberner, C., Tueckmantel, C., 2016. Anatomy and paleofluid evolution of laterally-restricted extensional fault zones in the Jabal Qusaybah anticline, Salakh Arc, Oman. Geological Society of America Bulletin, v. 128, p. 957–972, doi: 10.1130/B31317.1

Bertotti, G., Audra, P., Auler, A.S., Bezerra, F.H.R., de Hoop, S., Pontes, C., Prabhakaran, R., Lima, R., 2020. The Morro Vermelho Hypogenic Karst System: stratigraphy, fractures and flow in a carbonate strike-slip fault zone with implications for carbonate reservoir. Am. Assoc. Pet. Geol. Bull.

Boersma, Q., Prabhakaran, R., Bezerra, F.H., Bertotti, G., 2019. Linking natural fractures to karst cave development: a case study combining drone imagery, a natural cave network and numerical modelling. Pet. Geosci. 25(4), 454-469. https://doi.org/10.1144/petgeo2018-151

Cazarin, C.L., Bezerra, F.H.R., Borghi, L., Santos, R. V., Favoreto, J., Brod, J.A., Auler, A.S., Srivastava, N.K., 2019. The conduit-seal system of hypogene karst in Neoproterozoic carbonates in northeastern Brazil. Mar. Pet. Geol. 101, 90–107. https://doi.org/10.1016/j.marpetgeo.2018.11.046

Condie, K.C., 2002. The supercontinent cycle: Are there two patterns of cyclicity? J. African Earth Sci. 35, 179–183. https://doi.org/10.1016/S0899-5362(02)00005-2

Cosgrove, J.W., 2015. The association of folds and fractures and the link between folding, fracturing and fluid flow during the evolution of a fold-thrust belt: A brief review. Geol. Soc. Spec. Publ. 421, 41–68. https://doi.org/10.1144/SP421.11

Cruz, S.C.P., Alkmim, F.F., 2006. The tectonic interaction between the Paramirim aulacogen and the Araçuaí belt, São Francisco craton region, Eastern Brazil. An. Acad. Bras. Cienc. 78, 151–173. https://doi.org/10.1590/s0001-37652006000100014

D'Angeli, I.M., Parise, M., Vattano, M., Madonia, G., Galdenzi, S., De Waele, J., 2019. Sulfuric acid caves of Italy: A review. Geomorphology 333, 105–122. https://doi.org/10.1016/j.geomorph.2019.02.025

D'Angelo, T., Barbora, M. S. C., Danderfer Filho, A., 2019. Basement controls on cover deformation in eastern Chapada Diamantina, northern São Francisco Craton, Brazil: Insights from potential field data. Tectonophysics 772, 228-231. https://doi.org/10.1016/j.tecto.2019.228231

Davatzes, N.C., Aydin, A., 2003. Overprinting faulting mechanisms in high porosity sandstones of SE Utah. J. Struct. Geol. 25, 1795–1813. https://doi.org/10.1016/S0191-8141(03)00043-9

de Joussineau, G., Aydin, A., 2007. The evolution of the damage zone with fault growth in sandstone and its multiscale characteristics. J. Geophys. Res. Solid Earth 112, 1–19. https://doi.org/10.1029/2006JB004711 de Melo, M.S., Guimarães, G.B., Chinelatto, A.L., Giannini, P.C.F., Pontes, H.S., Chinelatto, A.S.A., Atencio, D., 2015. Kaolinite, illite and quartz dissolution in the karstification of Paleozoic sandstones of the Furnas Formation, Paraná Basin, Southern Brazil. J. South Am. Earth Sci. 63, 20–35. https://doi.org/10.1016/j.jsames.2015.06.011

De Waele, J., Fabbri, S., Santagata, T., Chiarini, V., Columbu, A., Pisani, L., 2018. Geomorphological and speleogenetical observations using terrestrial laser scanning and 3D photogrammetry in a gypsum cave (Emilia Romagna, N. Italy). Geomorphology 319, 47–61. https://doi.org/10.1016/j.geomorph.2018.07.012

De Waele, J., Plan, L., Audra, P., 2009. Recent developments in surface and subsurface karst geomorphology: An introduction. Geomorphology 106, 1–8. https://doi.org/10.1016/j.geomorph.2008.09.023

Dewever, B., Berwouts, I., Swennen, R., Breesch, L., Ellam, R.M., 2010. Fluid flow reconstruction in karstified Panormide platform limestones (north-central Sicily): Implications for hydrocarbon prospectivity in the Sicilian fold and thrust belt. Mar. Pet. Geol. 27, 939–958. https://doi.org/10.1016/j.marpetgeo.2009.10.018

Dublyansky, Y., 2012. Hydrothermal caves, Second Edi. ed, Encyclopedia of Caves. Elsevier Inc. https://doi.org/10.1016/B978-0-12-383832-2.00055-4

Dunham, R.J., 1962. Classification of Carbonate Rocks According to Depositional Textures. Classif. Carbonate Rocks--A Symp.

Ennes-Silva, R.A., Bezerra, F.H.R., Nogueira, F.C.C., Balsamo, F., Klimchouk, A., Cazarin, C.L., Auler, A.S., 2016. Superposed folding and associated fracturing influence hypogene karst development in Neoproterozoic carbonates, São Francisco Craton, Brazil. Tectonophysics 666, 244–259. https://doi.org/10.1016/j.tecto.2015.11.006

Evans, M.A., Fischer, M.P., 2012. On the distribution of fluids in folds: A review of controlling factors and processes. J. Struct. Geol. 44, 2–24. https://doi.org/10.1016/j.jsg.2012.08.003

Fabbri, S., Sauro, F., Santagata, T., Rossi, G., Waele, D., 2017. High-resolution 3-D mapping using terrestrial laser scanning as a tool for geomorphological and speleogenetical studies in caves: an example from the Lessini mountains (North Italy). Geomorphology 280, 16-29. https://doi.org/10.1016/j.geomorph.2016.12.001

Fischer, M., Wilkerson, M.S., 2000. Predicting the orientation of joints from fold shape: Results of pseudo – three-dimensional modeling and curvature analysis. Geology 28, 15-18. https://doi.org/10.1130/0091-7613(2000)28<15

Ford, D. C., and P. W. Williams *(*2007*),* Karst Hydrogeology and Geomorphology. John Wiley & Sons Ltd, The Atrium, Southern Gate, Chichester. England. https://doi.org/10.1002/9781118684986

Frumkin, A., 2013. New Developments of Karst Geomorphology Concepts. Treatise Geomorphol. 6, 1–13. https://doi.org/10.1016/B978-0-12-374739-6.00112-3

Gholpoiur, A.M., Cosgrove, J.W., Ala, M., 2016. New theoretical model for predicting and modelling fractures in folded fractured reservoirs. Pet. Geosci. 22, 257–280. https://doi.org/10.1144/petgeo2013-055

Gillespie, P.A., Howard, C.B., Walsh, J.J., Watterson, J., 1993. Measurement and characterisation of spatial distributions of fractures. Tectonophysics 226, 113–141. https://doi.org/10.1016/0040-1951(93)90114-Y

Giuffrida, A., La Bruna, V., Castelluccio, P., Panza, E., Rustichelli, A., Tondi, E., Giorgioni, M., Agosta, F., 2019. Fracture simulation parameters of fractured reservoirs: Analogy with outcropping carbonates of the Inner Apulian Platform, southern Italy. J. Struct. Geol. 123, 18–41. https://doi.org/10.1016/j.jsg.2019.02.007

Goldscheider, N., 2005. Fold structure and underground drainage pattern in the alpine karst system Hochifen-Gottesacker. Eclogae Geol. Helv. 98, 1–17. https://doi.org/10.1007/s00015-005-1143-z

Guerriero, V., Iannace, A., Mazzoli, S., Parente, M., Vitale, S., Giorgioni, M., 2010. Quantifying uncertainties in multi-scale studies of fractured reservoir analogues: Implemented statistical analysis of scan line data from carbonate rocks. J. Struct. Geol. 32, 1271–1278. https://doi.org/10.1016/j.jsg.2009.04.016

Guerriero, V., Vitale, S., Ciarcia, S., Mazzoli, S., 2011. Improved statistical multi-scale analysis of fractured reservoir analogues. Tectonophysics 504, 14–24. https://doi.org/10.1016/j.tecto.2011.01.003

Guimarães, J.T., Misi, A., Pedreira, A.J., Dominguez, J.M.L., 2011. The Bebedouro Formation, Una Group, Bahia (Brazil). Geol. Soc. Mem. 36, 503–508. https://doi.org/10.1144/M36.47

Jacquemyn, C., Swennen, R., Ronchi, P., 2012. Mechanical stratigraphy and (palaeo-) karstification of the Murge area (Apulia, southern Italy). Geol. Soc. London, Spec. Publ. 370, 169–186. https://doi.org/10.1144/SP370.4

Kim, Y.S., Sanderson, D.J., 2010. Inferred fluid flow through fault damage zones based on the observation of stalactites in carbonate caves. J. Struct. Geol. 32, 1305–1316. https://doi.org/10.1016/j.jsg.2009.04.017

Klimchouk, A., 2009. Morphogenesis of hypogenic caves. Geomorphology 106, 100–117. https://doi.org/10.1016/j.geomorph.2008.09.013

Klimchouk, A., Auler, A.S., Bezerra, F.H.R., Cazarin, C.L., Balsamo, F., Dublyansky, Y., 2016. Hypogenic origin, geologic controls and functional organization of a giant cave system in Precambrian carbonates, Brazil. Geomorphology 253, 385–405. https://doi.org/10.1016/j.geomorph.2015.11.002

Klimchouk, A., Palmer, A.N., De Waele, J., Auler, A.S., Audra, P., 2017. Hypogene Karst Regions and Caves of the World, Cave and Karst Systems of the World. Springer International Publishing, Cham. https://doi.org/10.1007/978-3-319-53348-3

La Bruna, V., Agosta, F., Prosser, G., 2017. New insights on the structural setting of the Monte Alpi area, Basilicata, Italy. Ital. J. Geosci. 136, 220–237. https://doi.org/10.3301/IJG.2017.03

La Bruna, V., Agosta, F., Lamarche, J., Viseur, S., Prosser, G., 2018. Fault growth mechanisms and scaling properties in foreland basin system: The case study of Monte Alpi, Southern Apennines, Italy. J. Struct. Geol. 116, 94–113. https://doi.org/10.1016/j.jsg.2018.08.009

La Bruna, V., Lamarche, J., Agosta, F., Rustichelli, A., Giuffrida, A., Salardon, R., Marié, L., 2020. Structural diagenesis of shallow platform carbonates: Role of early embrittlement on fracture setting and distribution, case study of Monte Alpi (Southern Apennines, Italy). J. Struct. Geol. 131. https://doi.org/10.1016/j.jsg.2019.103940

Lamarche, J., Gauthier, B.D.M., Ondicolberry, G., Fleury, J.T., 2018. Fracture Corridors in Fold and Thrust Zone, Devonian Sandstones Icla Syncline (Bolivia). In Third EAGE Workshop on Naturally Fractured Reservoirs (Vol. 2018, No. 1, pp. 1-5). European Association of Geoscientists & Engineers. https://doi.org/10.3997/2214-4609.201800022

Li, Y., Hou, G., Hari, K.R., Neng, Y., Lei, G., Tang, Y., Zhou, L., Sun, S., Zheng, C., 2018. The model of fracture development in the faulted folds: The role of folding and faulting. Mar. Pet. Geol. 89, 243–251. https://doi.org/10.1016/j.marpetgeo.2017.05.025

Ligtenberg, H., 2004. Fault seal analysis by enhancing fluid flow paths and fault irregularities in seismic data. AAPG Int. Conf., October 24-27, 2004, Cancun, Mexico.

Lyu, X., Zhu, G., Liu, Z., 2020. Well-controlled dynamic hydrocarbon reserves calculation of fracture–cavity karst carbonate reservoirs based on production data analysis. J. Pet. Explor. Prod. Technol. 10, 2401–2410. https://doi.org/10.1007/s13202-020-00881-w

Marrett, R., Ortega, O.J., Kelsey, C.M., 1999. Extent of power-law scaling for natural fractures in rock. Geology 27, 799–802. https://doi.org/10.1130/0091-7613(1999)027<0799:EOPLSF>2.3.CO

Matthäi, S.K., Belayneh, M., 2004. Fluid flow partitioning between fractures and a permeable rock matrix. Geophys. Res. Lett. 31, L07602 https://doi.org/10.1029/2003GL019027

Mazzoli, S., Ascione, A., Buscher, J.T., Pignalosa, A., Valente, E., Zattin, M., 2014. Low-angle normal faulting and focused exhumation associated with late Pliocene change in tectonic style in the southern Apennines (Italy). Tectonics 33, 1802–1818. https://doi.org/10.1002/2014TC003608

Menezes, C., Martins Compan, A.L., Surmas, R., 2016. Permeability estimation using ultrasonic borehole image logs in dual-porosity carbonate reservoirs. Petrophysics 57, 620–637.

Miranda, T.S., Barbosa, J.A., Gale, J.F.W., Marrett, R., Gomes, I., Neumann, V.H.L.M., Matos, G.C., Correia, O.J., Alencar, M.L., 2014. Natural Fracture Characterization in Aptian Carbonates, Araripe Basin, NE Brazil, in: 76th EAGE Conference & Exhibition. Amsterdam, The Netherlands.

Misi, A., Veizer, J., 1998. Neoproterozoic carbonate sequences of the Una Group, Irecê Basin, Brazil: chemostratigraphy, age and correlations. Precambrian Res. 89, 87–100. https://doi.org/10.1016/S0301-9268(97)00073-9

Montaron, B., 2008. Confronting Carbonates, in: Oil Review Middle East. Abu Dhabi.

Morley, C.K., Warren, J., Tingay, M., Boonyasaknanon, P., Julapour, A., 2014. Comparison of modern fluid distribution, pressure and flow in sediments associated with anticlines growing in deepwater (Brunei) and continental environments (Iran). Mar. Pet. Geol. 55, 230–249. https://doi.org/10.1016/j.marpetgeo.2014.01.013

Myers, R., Aydin, A., 2004. The evolution of faults formed by shearing across joint zones in sandstone. J. Struct. Geol. 26, 947–966. https://doi.org/10.1016/j.jsg.2003.07.008

Mylroie, J.E., 2012. Coastal caves, Second Edi. ed, Encyclopedia of Caves. Elsevier Inc. https://doi.org/10.1016/B978-0-12-383832-2.00022-0

Narasimhan, T.N., 2005. Hydrogeology in North America: Past and future. Hydrogeol. J. 13, 7–24. https://doi.org/10.1007/s10040-004-0422-5

Odling, N.E., Gillespie, P., Bourgine, B., Castaing, C., Chilés, J.P., Christensen, N.P., Fillion, E., Genter, A., Olsen, C., Thrane, L., Trice, R., Aarseth, E., Walsh, J.J., Watterson, J., 1999. Variations in fracture system geometry and their implications for fluid flow in fractured hydrocarbon reservoirs. Pet. Geosci. 5, 373–384. https://doi.org/10.1144/petgeo.5.4.373

Odonne, F., Lézin, C., Massonnat, G., Escadeillas, G., 2007. The relationship between joint aperture, spacing distribution, vertical dimension and carbonate stratification: An example from the Kimmeridgian limestones of Pointe-du-Chay (France). J. Struct. Geol. 29, 746–758. https://doi.org/10.1016/j.jsg.2006.12.005

Ogata, K., Senger, K., Braathen, A., Tveranger, J., Olaussen, S., 2012. The importance of natural fractures in a tight reservoir for potential CO_2 storage: a case study of the upper Triassic–middle Jurassic Kapp Toscana Group (Spitsbergen, Arctic Norway). Geol. Soc. London, Spec. Publ. 374, 395–415. https://doi.org/10.1144/sp374.9

Ogata, K., Senger, K., Braathen, A., Tveranger, J., 2014. Fracture corridors as seal-bypass systems in siliciclastic reservoir-cap rock successions: Field-based insights from the Jurassic Entrada Formation (SE Utah, USA). J. Struct. Geol. 66, 162–187. https://doi.org/10.1016/j.jsg.2014.05.005

Ortega, O.J., Marrett, R.A., Laubach, S.E., 2006. A scale-independent approach to fracture intensity and average spacing measurement. Am. Assoc. Pet. Geol. Bull. 90, 193–208. https://doi.org/10.1306/08250505059

Palmer, A., 1990. Groundwater processes in karst terrains. In: Higgins C.G. & Coates D.R. (Eds.), Groundwater geomorphology; the role of subsurface water in Earth-Surface processes and landforms. GSA Special Papers 252, 177-209. https://doi.org/10.1130/SPE252-p177

Pantou, I., 2014. Impact of stratigraphic heterogeneity on hydrocarbon recovery in carbonate reservoirs: Effect of karst. Imperial College London.

Panza, E., Agosta, F., Zambrano, M., Tondi, E., Prosser, G., Giorgioni, M., Janiseck, J.M., 2015. Structural architecture and discrete fracture network modelling of layered fractured carbonates (Altamura Fm., Italy). Ital. J. Geosci. 134, 409–422. https://doi.org/10.3301/IJG.2014.28

Peacock, D.C.P., Shepherd, J., Peacock, D.C.P., 1997. Reactivated faults and transfer zones in the Southern Coalfield, Sydney Basin, Australia. Aust. J. Earth Sci. 44, 265–273. https://doi.org/10.1080/08120099708728309

Pollard, D.D., Aydin, A., 1988. Progress in understanding jointing over the past century. Spec. Pap. Geol. Soc. Am. 253, 313–336. https://doi.org/10.1130/SPE253-p313

Pollastro, R.M., 2003. Total Petroleum Systems of the Paleozoic and Jurassic, Greater Ghawar Uplift and Adjoining Provinces of Central Saudi Arabia and Northern Arabian-Persian Gulf U.S. Geological Survey Bulletin 2202-H Total Petroleum Systems of the Paleozoic and Jurassic, US Geological Survey 2202-H.

Pontes, C.C.C., Nogueira, F.C.C., Bezerra, F.H.R., Balsamo, F., Miranda, T.S., Nicchio, M.A., Souza, J.A.B., Carvalho, B.R.B.M., 2019. Petrophysical properties of deformation bands in high porous sandstones across fault zones in the Rio do Peixe Basin, Brazil. Int. J. Rock Mech. Min. Sci. 114, 153–163. https://doi.org/10.1016/j.ijrmms.2018.12.009

Popov, P., Qin, G., Bi, L., Efendiev, Y., Ewing, R., Kang, Z., Li, J., 2007. Multiscale methods for modeling fluid flow through naturally fractured carbonate karst reservoirs. Proc. - SPE Annu. Tech. Conf. Exhib. 6, 3714–3722. https://doi.org/10.2523/110778-ms

Questiaux, J.-M., Couples, G., Ruby, N., 2010. Fractured reservoirs with fracture corridors. Geophys. Prospect. 58, 279–295. https://doi.org/1365-2478.2009.008140.x

Railsback, L.B., 1998. Evaluation of spacing of stylolites and its implications for self-organization of pressure dissolution. J. Sediment. Res. 68, 2–7. https://doi.org/10.2110/jsr.68.2

Ramsay, J.G., 1967. Folding and Fracturing of Rocks. McGraw-Hill, New York, pp. 568.

Santos, R.F.V.C., Miranda, T.S., Barbosa, J.A., Gomes, I.F., Matos, G.C., Gale, J.F.W., Neumann, V.H.L.M., Guimarães, L.J.N., 2015. Characterization of natural fracture systems: Analysis of uncertainty effects in linear scanline results. Am. Assoc. Pet. Geol. Bull. 99, 2203–2219. https://doi.org/10.1306/05211514104

Segall, P., Pollard, D.P., 1983. Nucleation and growth of strike slip faults in granite. J. Geophys. Res. 88, 555–568. https://doi.org/10.1029/JB088iB01p00555

Souque, C., Knipe, R.J., Davies, R.K., Jones, P., Welch, M.J., Lorenz, J., 2019. Fracture corridors and fault reactivation: Example from the Chalk, Isle of Thanet, Kent, England. J. Struct. Geol. 122, 11–26. https://doi.org/10.1016/j.jsg.2018.12.004

Terzaghi, R.D., 1965. Sources of Error in Joint Surveys. Géotechnique 15, 287–304. https://doi.org/10.1680/geot.1965.15.3.287

Tian, F., Lu, X., Zheng, S., Zhang, H., Rong, Y., Yang, D., Liu, N., 2017. Structure and Filling Characteristics of Paleokarst Reservoirs in the Northern Tarim Basin, Revealed by Outcrop, Core and Borehole Images. Open Geosci. 9, 266–280. https://doi.org/10.1515/geo-2017-0022

Tian, F., Zhang, H., Zheng, S., Lei, Y., Rong, Y., Lu, X., Jin, Q., Zhang, L., Liu, N., 2015. Multi-layered ordovician paleokarst reservoir detection and spatial delineation: A case study in the Tahe Oilfield, Tarim Basin, Western China. Mar. Pet. Geol. 69, 53–73. https://doi.org/10.1016/j.marpetgeo.2015.10.015

Tisato, N., Sauro, F., Bernasconi, S.M., Bruijn, R.H.C., De Waele, J., 2012. Geomorphology Hypogenic contribution to speleogenesis in a predominant epigenic karst system: A case study from the Venetian Alps, Italy. Geomorphology 151–152, 156–163. https://doi.org/10.1016/j.geomorph.2012.01.025

Wang, X., Lei, Q., Lonergan, L., Jourde, H., Gosselin, O., Cosgrove, J., 2017. Heterogeneous fluid flow in fractured layered carbonates and its implication for generation of incipient karst. Adv. Water Resour. 107, 502–516. https://doi.org/10.1016/j.advwatres.2017.05.016

Warren, J., Morley, C.K., Charoentitirat, T., Cartwright, I., Ampaiwan, P., Khositchaisri, P., Mirzaloo, M., Yingyuen, J., 2014. Structural and fluid evolution of Saraburi Group sedimentary carbonates, central Thailand: A tectonically driven fluid system. Mar. Pet. Geol. 55, 100–121. https://doi.org/10.1016/j.marpetgeo.2013.12.019

Wilson, C.E., Aydin, A., Durlofsky, L.J., Sagy, A., Emily, E., Kreylos, O., Kellogg, L.H., 2011. From outcrop to flow simulation: Constructing discrete fracture models from a LIDAR survey. Am. Assoc. Pet. Geol. Bull. 95, 1883–1905. https://doi.org/10.1306/03241108148

Worthington, S.R.H., Ford, D.C., 1995. High sulfate concentrations in limestone springs: An important factor in conduit initiation? Environ. Geol. 25, 9–15.

Xu, X., Chen, Q., Chu, C., Li, G., 2017. Tectonic evolution and paleokarstification of carbonate rocks in the Paleozoic Tarim Basin. Carbonates and Evaporites 32, 487–496. https://doi.org/10.1007/s13146-016-0307-4

Zambrano, M., Tondi, E., Korneva, I., Panza, E., Agosta, F., Janiseck, J.M., Giorgioni, M., 2016. Fracture properties analysis and discrete fracture network modelling of faulted tight limestones, Murge Plateau, Italy. Ital. J. Geosci. 135, 55-67. https://doi.org/10.3301/IJG.2014.42

Zhao, K., Zhang, L., Zheng, D., Sun, C., Dang, Q., 2015. A reserve calculation method for fracture-cavity carbonate reservoirs in Tarim Basin, NW China. Pet. Explor. Dev. 42, 277–282. https://doi.org/10.1016/S1876-3804(15)30017-3

Figure caption

Figure 1. (a) Sketch map of the São Francisco Craton Salitre formation; (b) zoom and location of the studied sites.

Figure 2. (a) Schematic stratigraphic column of the study area from Ioiô, Lapinha, Torrinha, and Paixão caves. (b) close up view of a grainstone; (c) photomicrograph of a representative mudstone with the pervasive occurrence of pyrite. (d) hand sample of mudstone with siltstone levels; (e) photomicrograph of mudstone that shows siliciclastic grains; (e) close up view of mudstone with chert nodules; (g) photomicrograph of a representative grainstone; Key: Un: stratigraphic unit described in the text, M: Mudstone, W: Wackestone, P: Packstone, G: Grainstone, F: Floatstone, Py: pyrite, Si: Silica, dol: dolomite, S0: bedding.

Figure 3. 3D model slice orthogonal to the cave passage in Ioiô cave showing different levels of dissolution due to distinct carbonate rock textures. The location of the slice is shown in Fig. 7b. Key: FCZ: fracture corridor zone; HDZ: high-dissolution zone; SdB: Sedimentary breccia; MdSL: Mudstone with Silstone level; Md: mudstone; St: stalactites.

Figure 4. (a) View of the Ioiô cave roof displaying speleothems aligned along the main N-S- and E-W-striking fracture zones; (b) Orthogonal system of fractures on the cave ceiling; (c) gentle fold highlighting the high dissolution zone along the fold hinge. Note opposite bedding dips. Key: HDZ: high-dissolution zone.

Figure 5. (a) outcrop view of an external wall near Lapinha cave entrance; (b) linedrawing of (a); (c) lower hemisphere equal-area projections of the poles related to the NSB and SB; (d) close up view of a karst dissolution zone parallel to a persistent non-stratabound fracture zone inside the cave. Key: NSB = Non-Stratabound fracture; S0 = bedding.

Figure 6. Close up view of fracture sets in the ceiling of caves: (a) E-W-striking fracture set abuts against N-S-striking fracture set in the Torrinha cave; (b) bed-parallel stylolite and bedperpendicular folded vein in the Ioiô cave; (c) normal fault with left-lateral strike-slip kinematics in the Lapinha cave; (d) line drawing of (c).

Figure 7. Structural and karst features of the Ioiô cave: (a) cave map with area surveyed with LiDAR; (b) 3D LiDAR model of the cave with the location of investigated sites; (c) main fold hinges of the cave; (d) lower hemisphere equal-area projection of the poles and relative density contour plots of bedding planes and fractures; (e) digital image of the slice on site B showing a high dissolution zone along a fracture corridor following the fold hinge in the central part of the cave passage; (f) detail of HDZ highlighted in (e) (yellow square). Key: FCZ: fracture corridor zone; HDZ: high-dissolution zone.

Figure 8. Structural and karst features of the Lapinha cave: (a) cave map with area surveyed with LiDAR; (b) 3D model of the cave with the location of investigated sites; (c) structural map of the central part of the cave showing two main directions of anticline folds (d) lower hemisphere equalarea projection of the poles of NSB and SB fractures, mean bedding planes, and mean fold hinge (black dot); (e) digital slice between the (C) and (I) sites highlighting the wavelength of N-S folds. Key: FCZ: fracture corridor zone.

Figure 9. Geometric features of the Torrinha (a-d) and Paixão (e) caves: (a) internal view of the cave geometry showing widening of the passage along the fold hinge; (b) 3D LiDAR model (a); (c) plan view of the site (e) (location in Fig. 9b) showing both major N-S- and subsidiary E-Woriented cave passages; (d) transversal view of (d) showing the vertical elliptical shape of

the cave passages; (e) 3D LiDAR model of Paixão cave ceiling with a close up view of two N-S- and E-W-string fracture sets.

Figure 10. Structural and dissolutional features of the Torrinha cave: (a) map highlighting the LiDAR surveyed area in the southern portion of the cave; (b) 3D model of the scanned areas with the location of investigated sites; (c) structural map of site B in the cave; (d) lower hemisphere equal-area projection of the poles of NSB and SB fractures, mean bedding planes, and mean fold hinge (black dot). (e) NW-SE strike-slip fault at site B of Torrinha cave.

Figure 11. Structural and dissolutional features of the Paixão cave: (a) map highlighting the area surveyed with LiDAR and location of the investigated sites; (b) 3D LiDAR model of the studied part of the cave; (c) structural map of the eastern part of the Paixão cave highlighting the en echelon pattern of fold hinges; (d) lower hemisphere equal-area projection of the poles of NSB and SB fractures, mean bedding planes, and mean fold hinge (black dot); (e) zoom on the central portion of the model highlighting the location of a fault zone (blue ellipsoid); (f) digital slice of the cave's central portion affected by a dip-slip fault zone; (g) orthogonal-to-dip view of a normal fault located in the central portion of the cave; (h) cave central portion highlighting the fault displayed in (e). Key: HD = High displacement;St = stalactite.

Figure 12. Quantitative data of the Ioiô site: (a) Outcrop oblique view of the site and the investigated beds; red lines used for the linedrawings are related to both SB and NSB fractures; (b) Lower hemisphere equal-area projection of the poles and relative density contour plots representing the fractures measured in the site; (c) Log-log diagrams of the cumulative frequency distribution for fracture spacing; blue lines correspond to exponential-law

distribution, red lines correspond to power-law distribution calculated for the single fracture sets in the site.

Figure 13. Quantitative data in the Lapinha site: (a) Outcrop view of beds; red lines used for the linedrawing are related to both SB and NSB fracture sets; (b) Lower hemisphere equal-area projection of poles and relative density contour plots representing fractures; (c) Log-log diagram of the cumulative frequency distribution for fracture spacing; blue lines correspond to exponentiallaw distribution, red lines correspond to power-law distribution calculated for the single fracture sets.

Figure 14. Quantitative structural data of the Torrinha site: (a) Outcrop view of the investigated beds outside the cave; red lines used for the linedrawing are related to both SB and NSB fractures; (b) lower hemisphere equal-area projection of the poles and relative density contour plots representing the fractures; (c) log-log diagrams of the cumulative frequency distribution for fracture spacing; blue lines correspond to exponential law distribution and red lines correspond to power-law distribution calculated for the single fracture sets in the site.

Figure 15. Quantitative data for the Paixão site: (a) lower hemisphere equal-area projection of the poles and relative density contour plots representing the fractures; (b) log-log diagram of the cumulative frequency distribution for fracture spacing; blue lines correspond to exponential-law distribution; red lines correspond to power-law distribution calculated for the single fracture sets in the site.

Figure 16. Evolutionary conceptual model proposed for development of the hypogenic conduits in carbonate units of the Salitre Formation, Brazil. (a) background burial-related; (b) E-W compression; (c) N-S compression; (d) ascending fluids and karst development

Figure 1

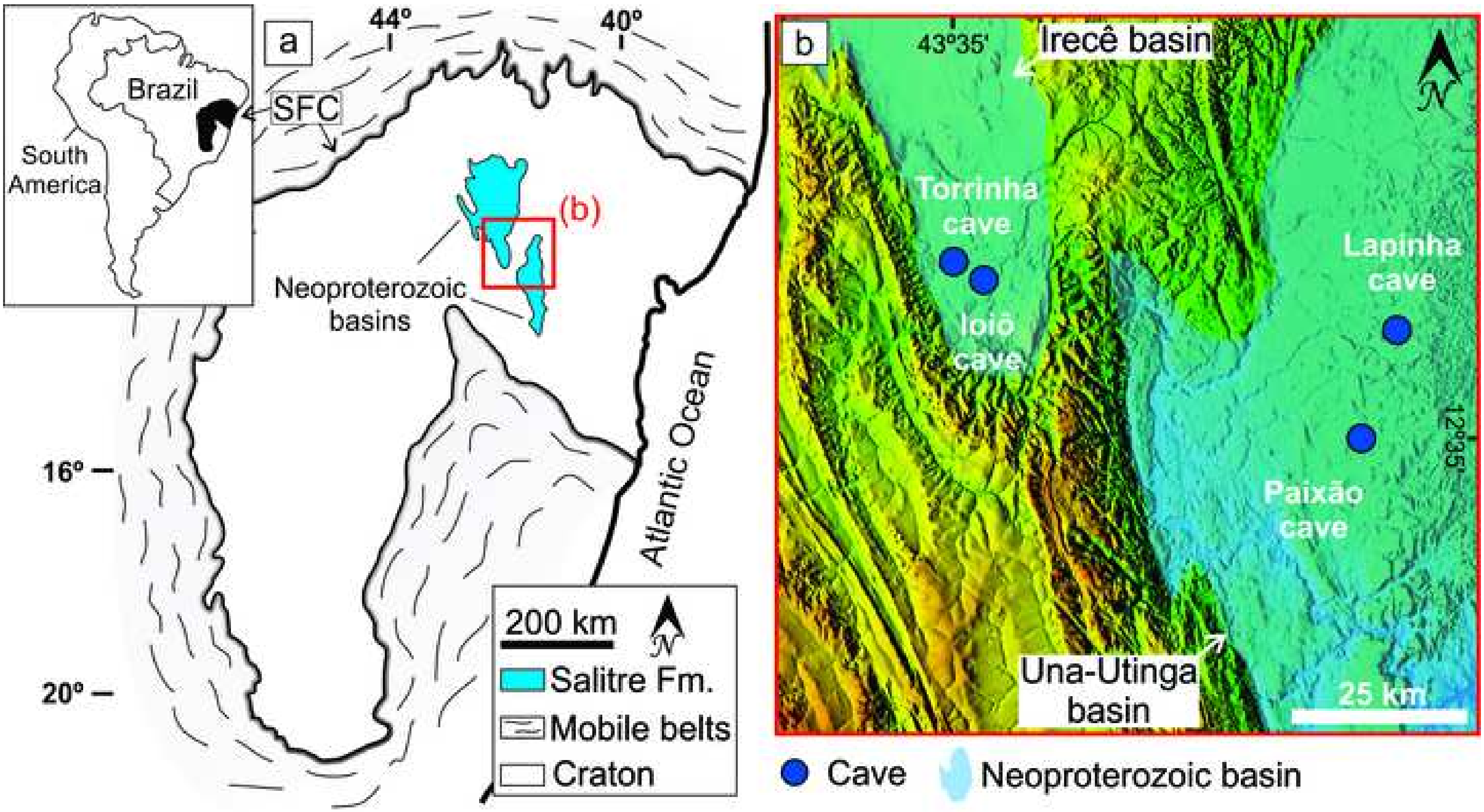

a
44°
40°
Brazil
SFC
South America
(b)
Neoproterozoic basins
16°
20°
Atlantic Ocean
200 km
Salitre Fm.
Mobile belts
Craton
b
43°35'
Irecê basin
Torrinha cave
Ioiô cave
Lapinha cave
12°35'
Paixão cave
Una-Utinga basin
25 km
Cave
Neoproterozoic basin

Figure 2 Click here to access/download;Figure;2 petrografia.jpg

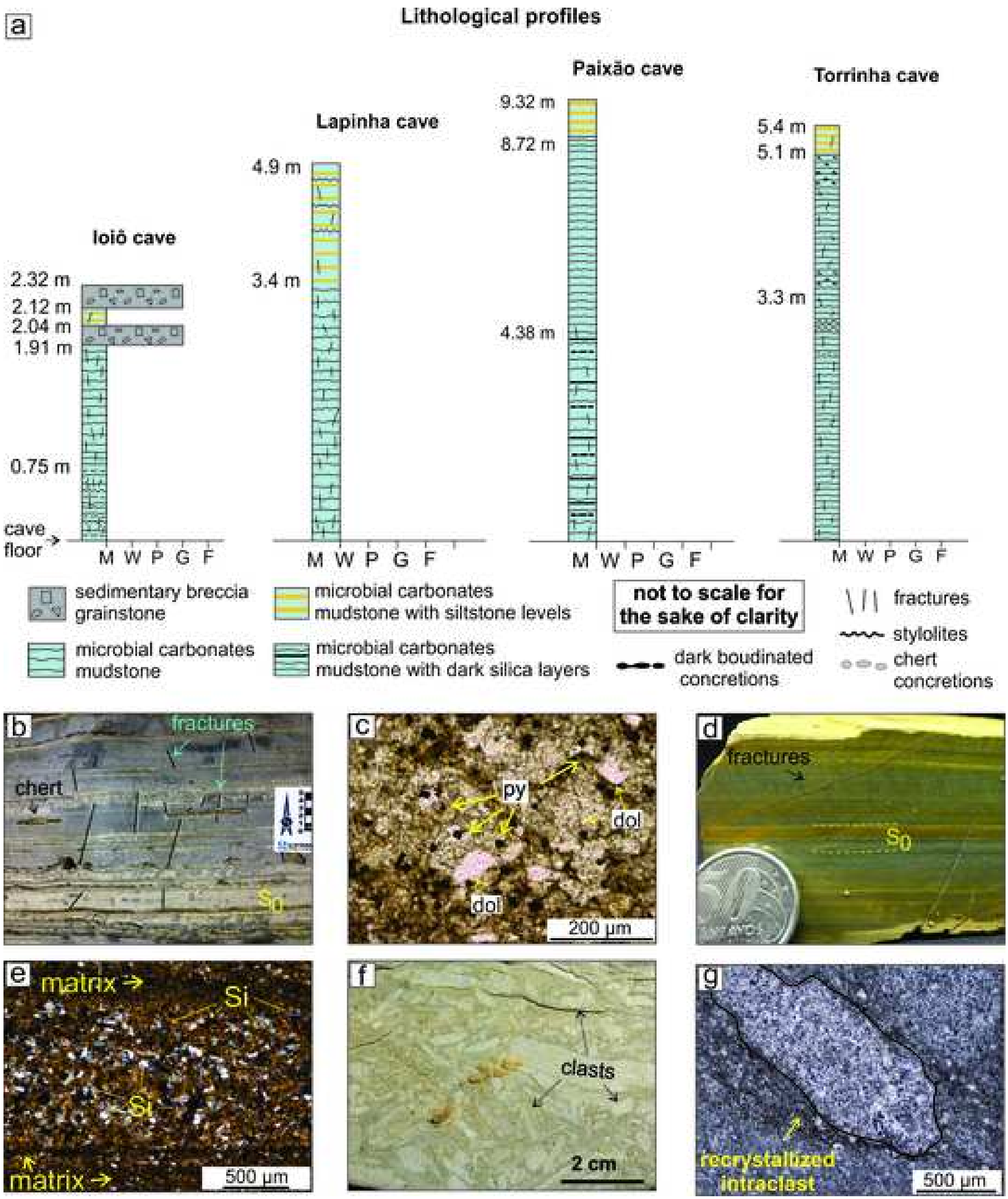

Figure 3

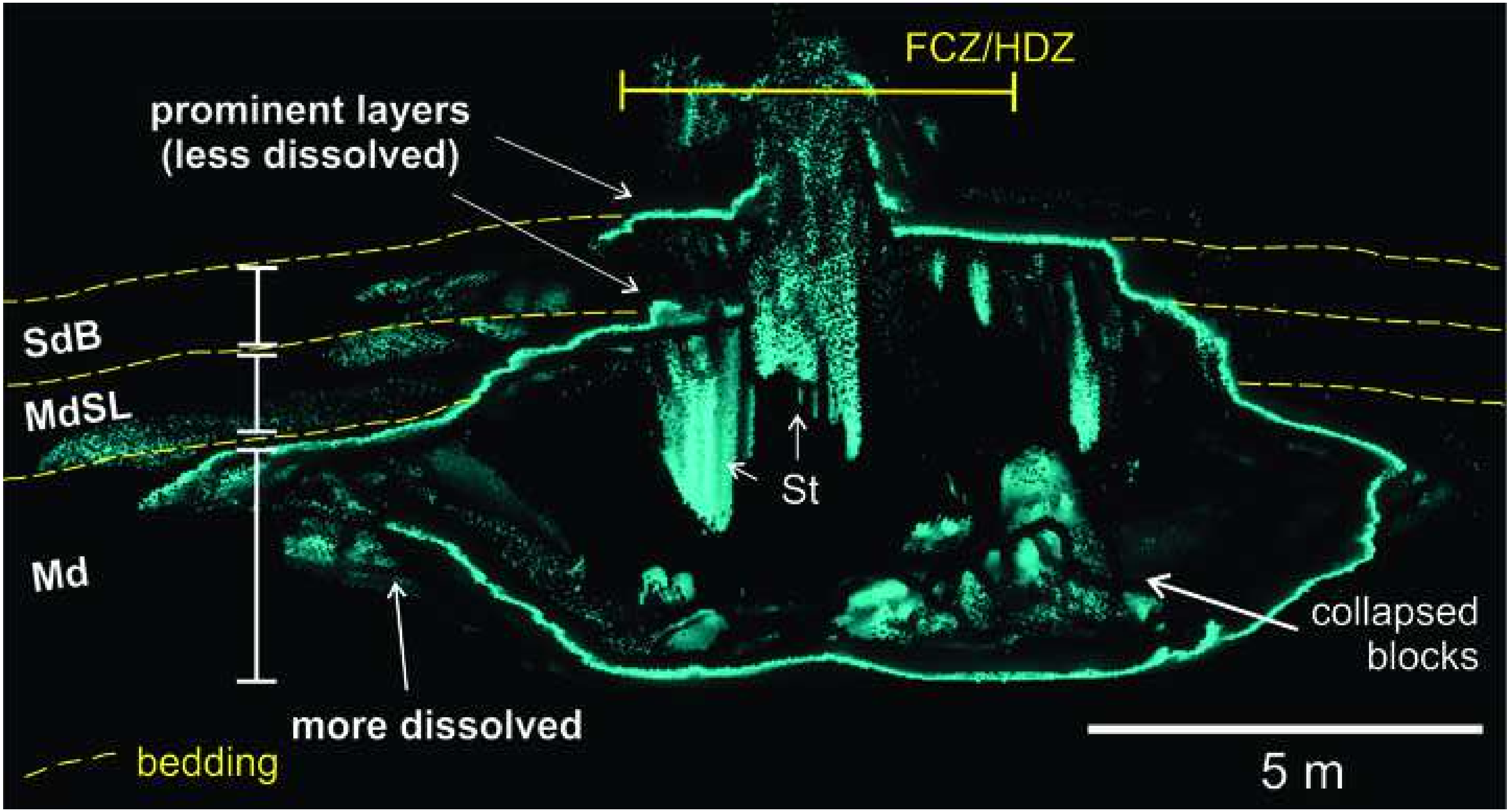
FCZ/HDZ
prominent layers
(less dissolved)
SdB
MdSL
Md
St
collapsed
blocks
more dissolved
bedding
5 m

Figure 4

Click here to access/download;Figure;4 fractures ioio.jpg

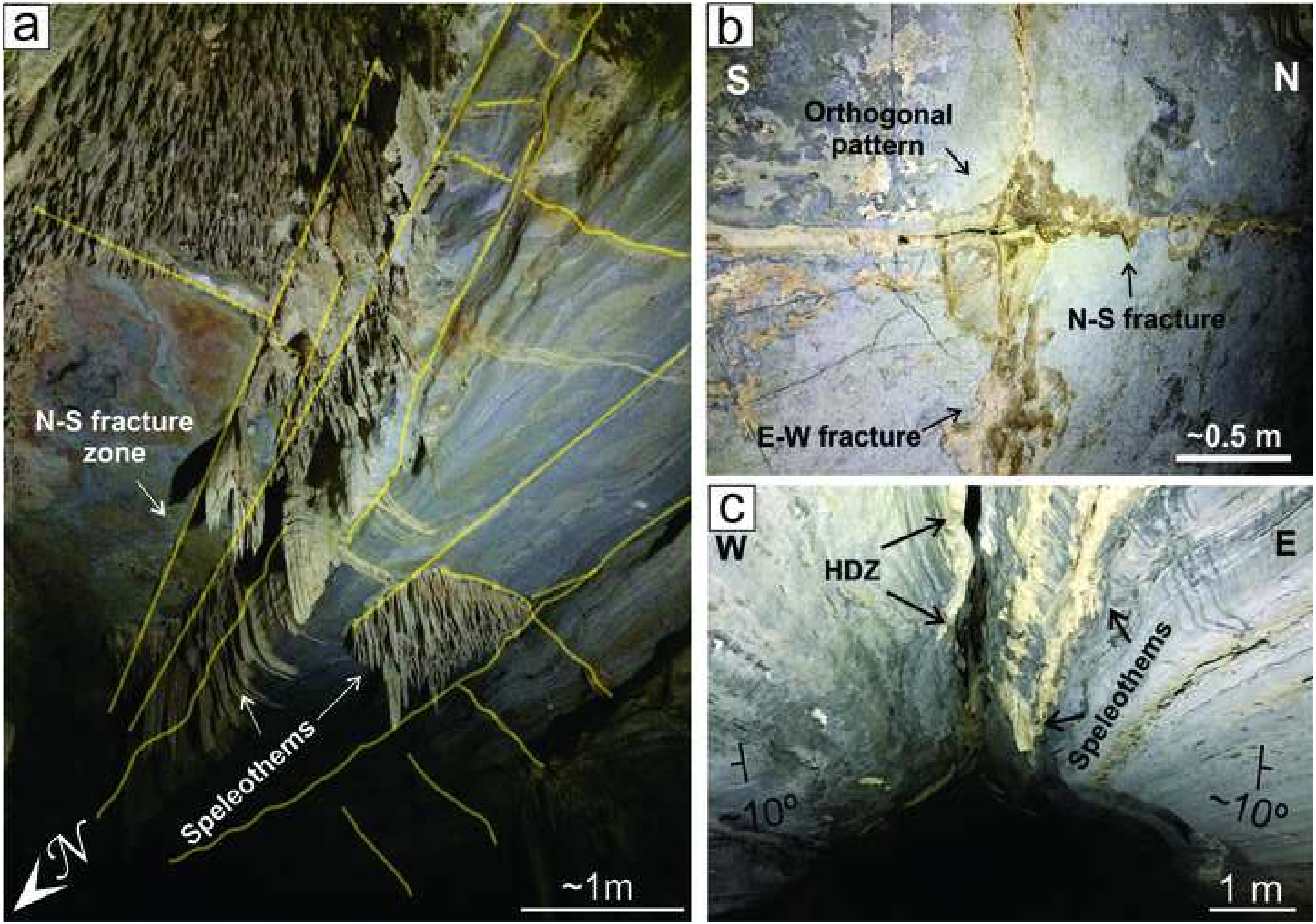

Figure 5

Click here to access/download;Figure;5 Lapinha outside.jpg

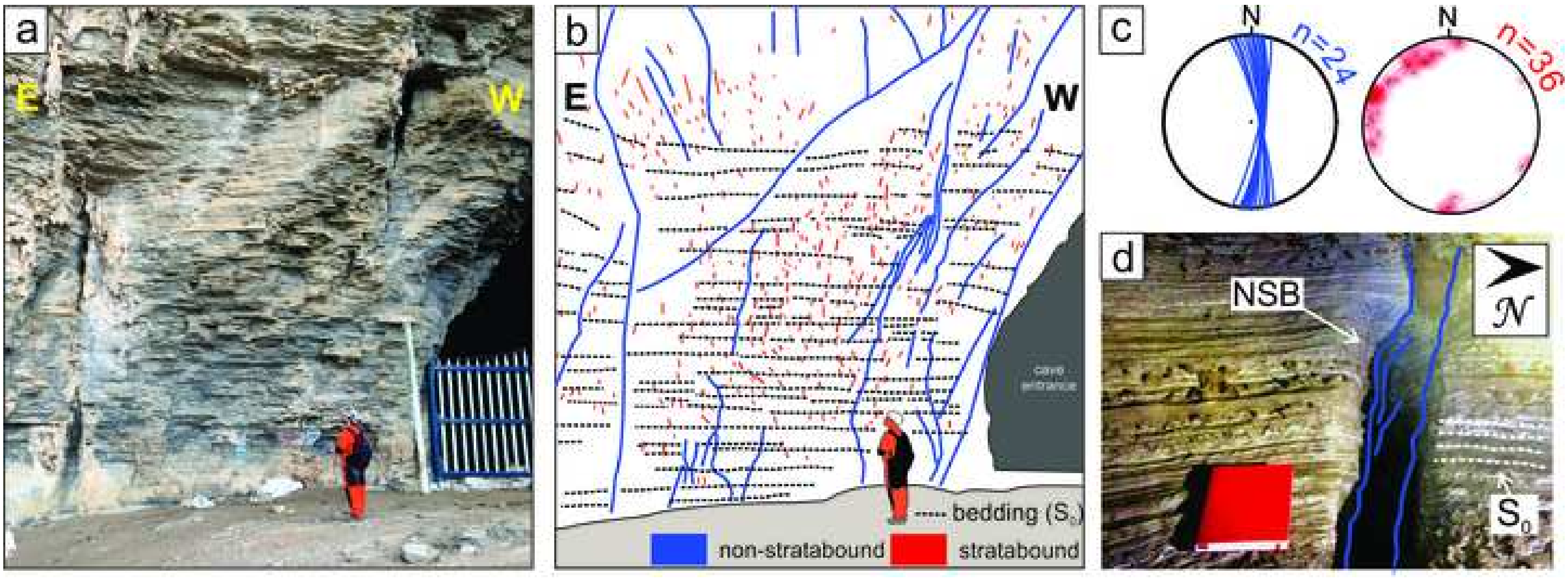

Figure 6

Click here to access/download;Figure;6 stylolites.jpg

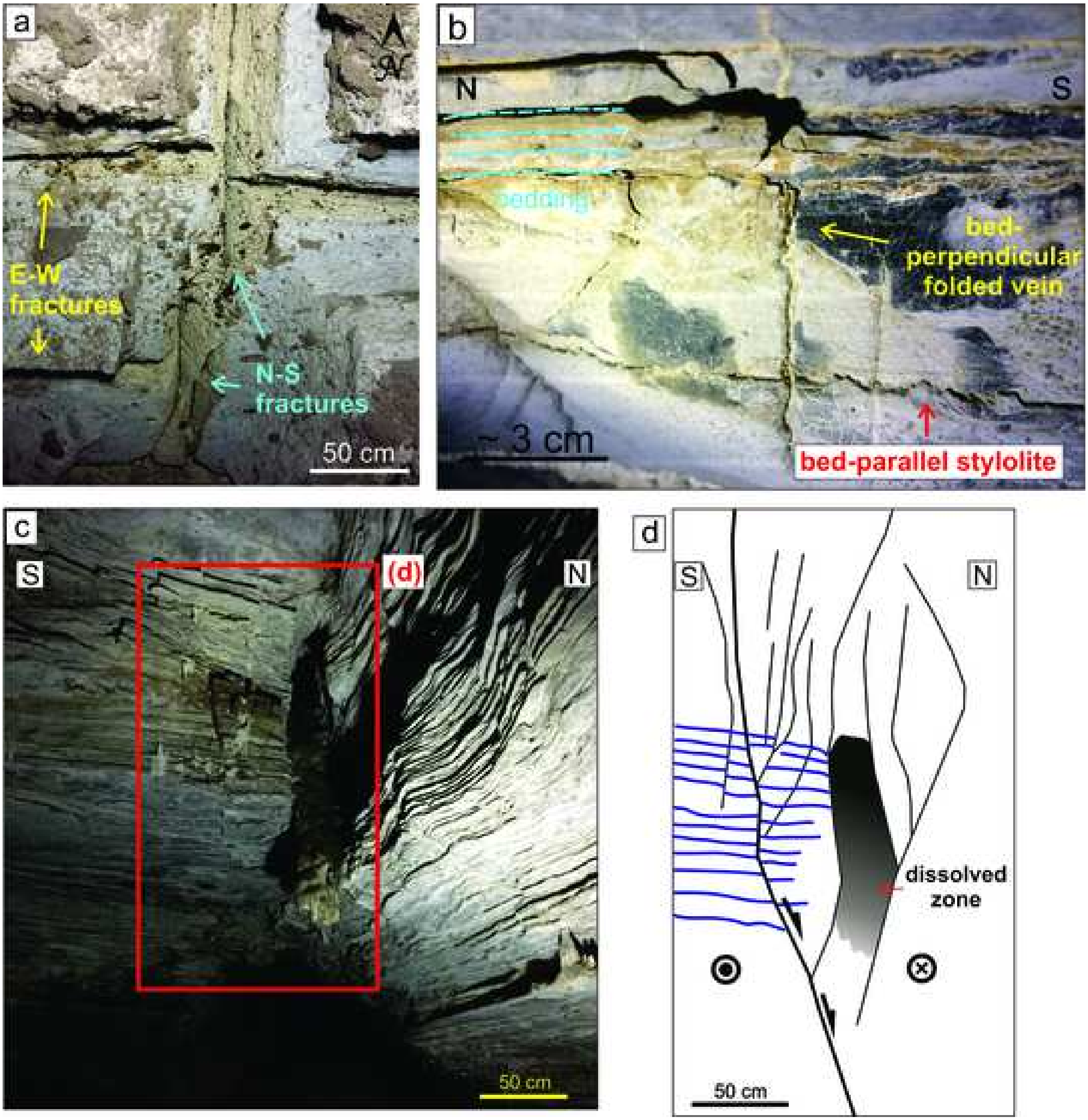

Figure 7

Click here to access/download;Figure;7 ioio cave.jpg

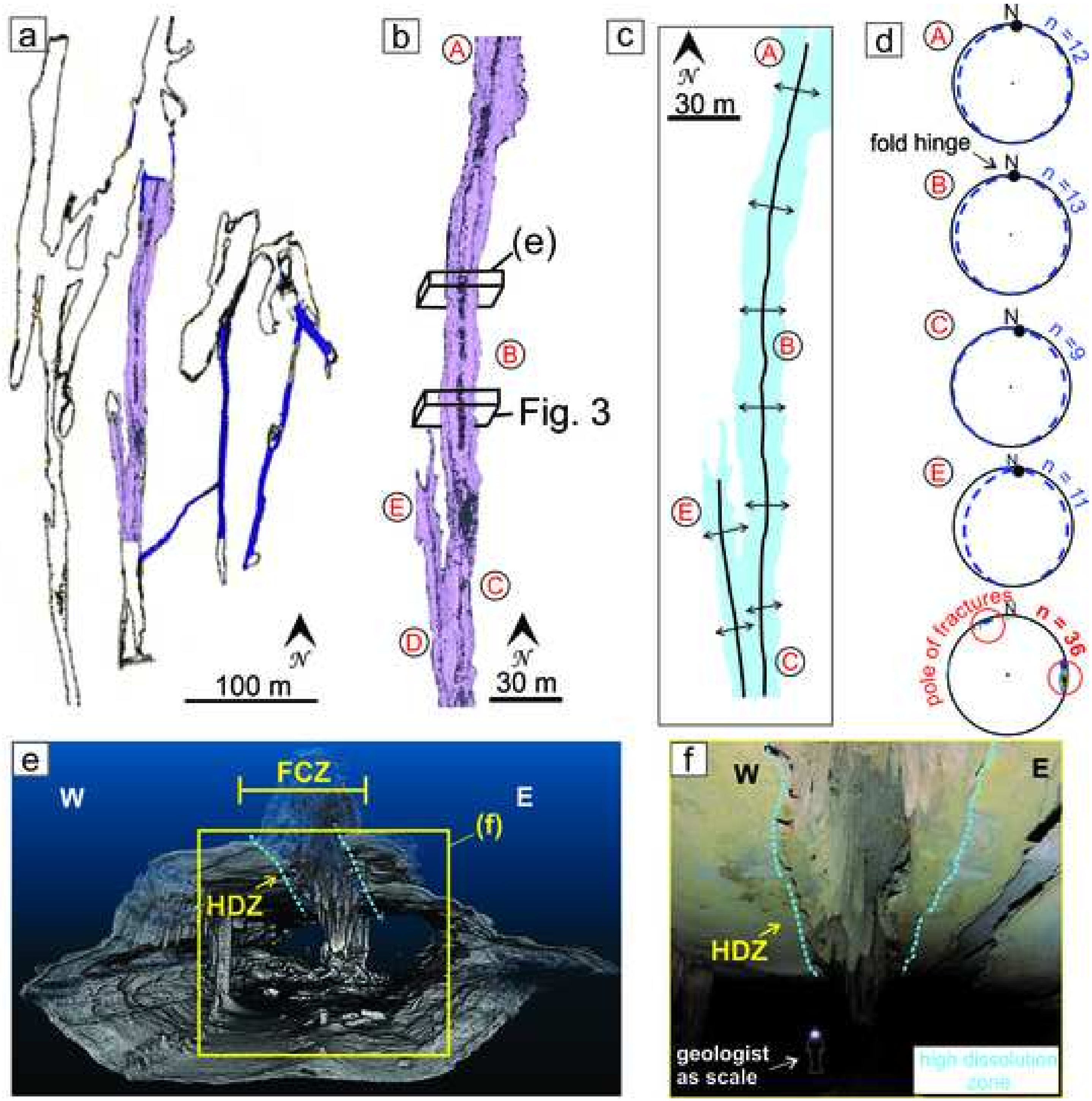

Figure 8 Click here to access/download;Figure;8 lapinha cave.jpg

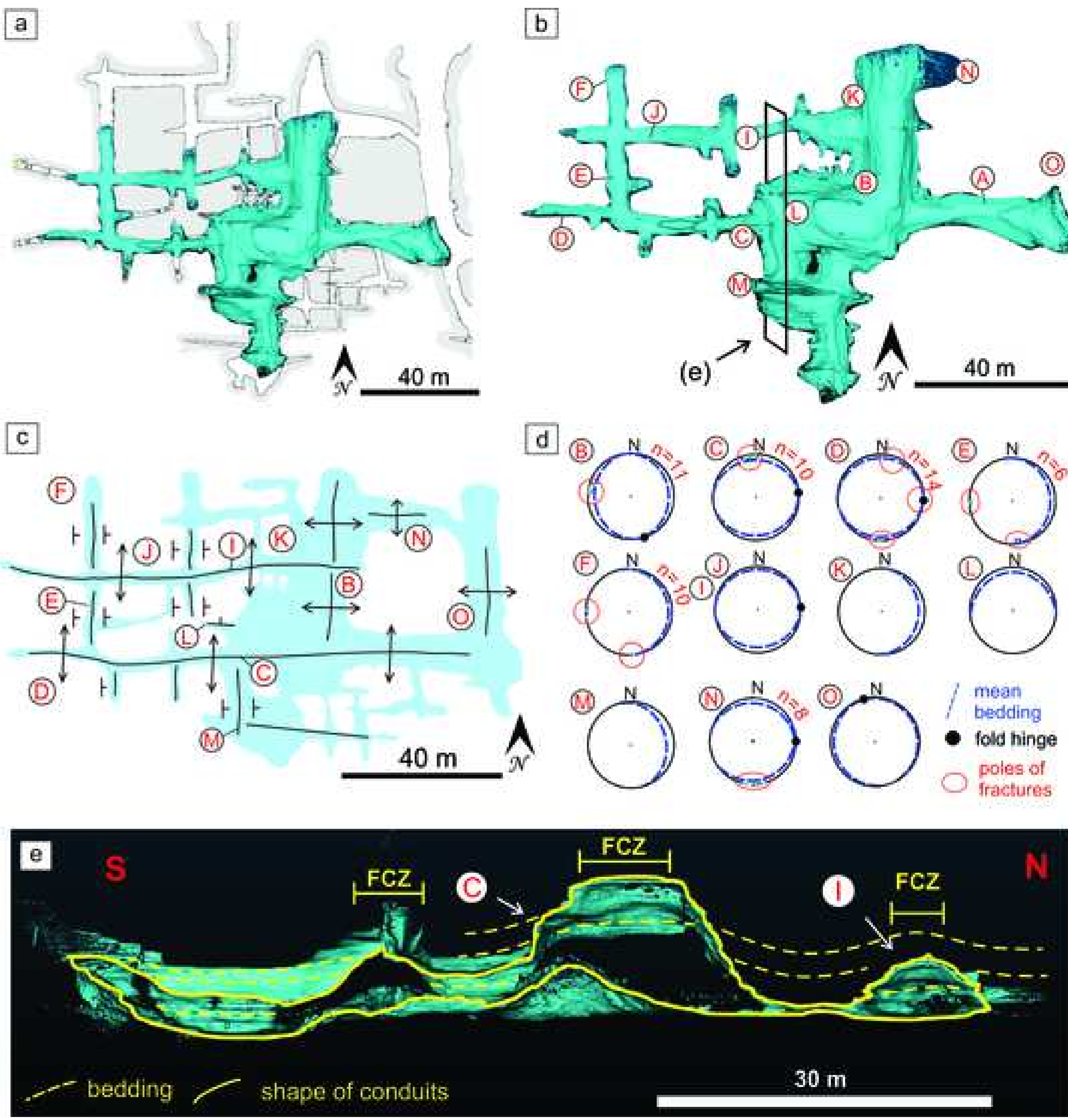

Figure 9

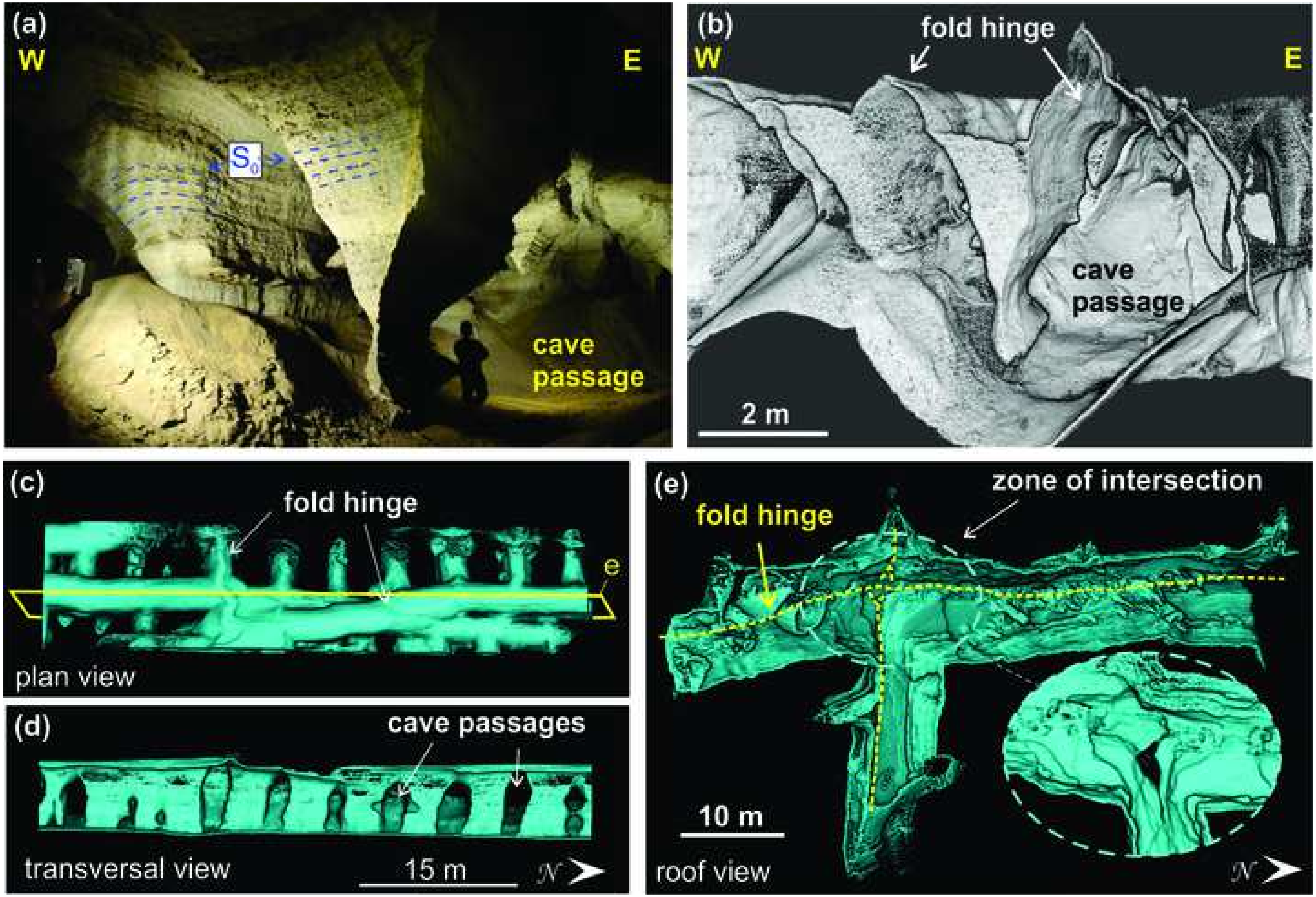
(a)
W
E
S_0
cave passage
(b)
W
fold hinge
E
cave passage
2 m
(c)
fold hinge
e
plan view
(d)
cave passages
transversal view
15 m
N
(e)
zone of intersection
fold hinge
10 m
roof view
N

Figure 10

Click here to access/download;Figure;10 Torrinha line drawning.jpg

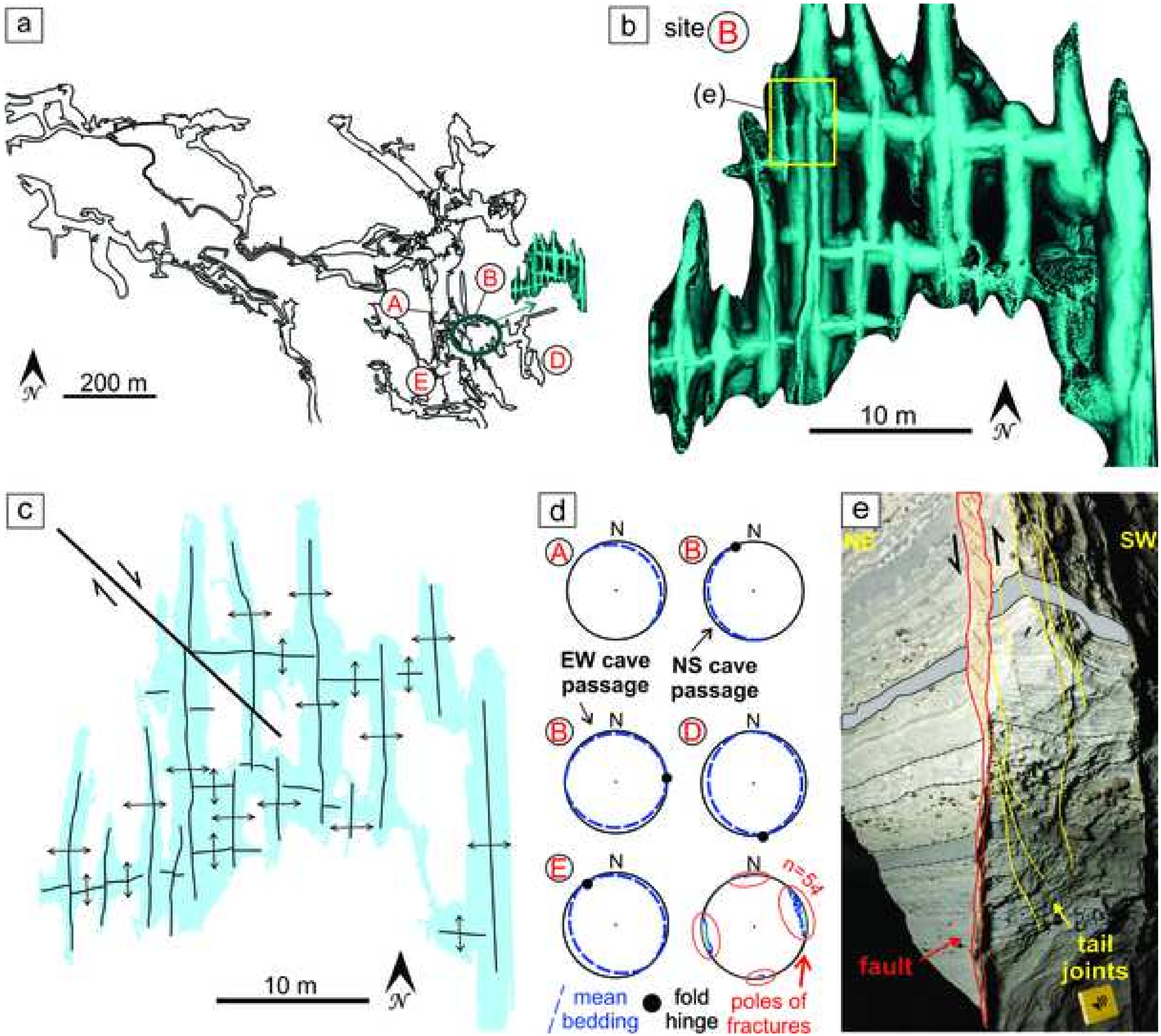

Figure 11 Click here to access/download;Figure;11 paixas.jpg

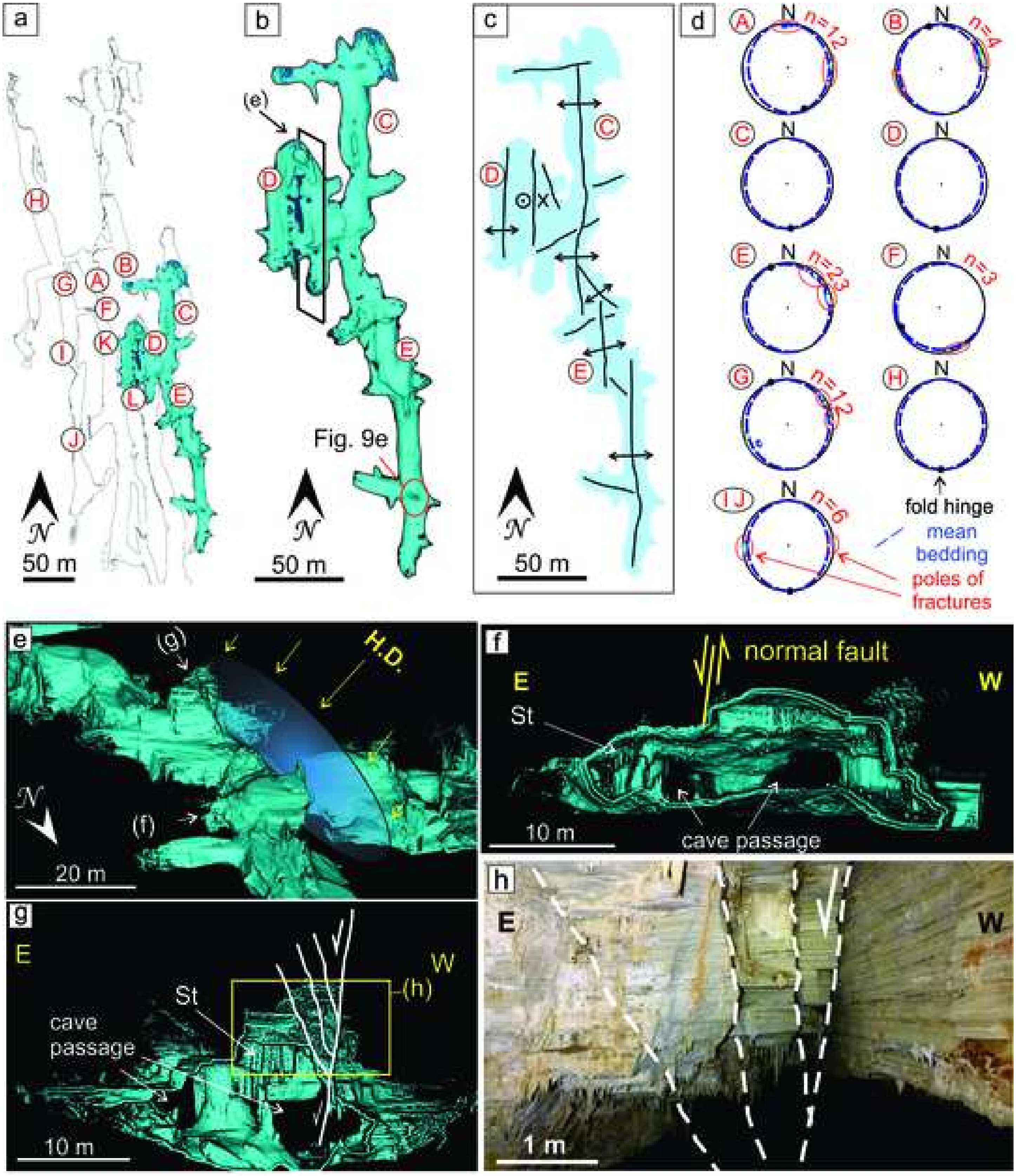

Figure 12

Click here to access/download;Figure;12 Ioio figure.jpg

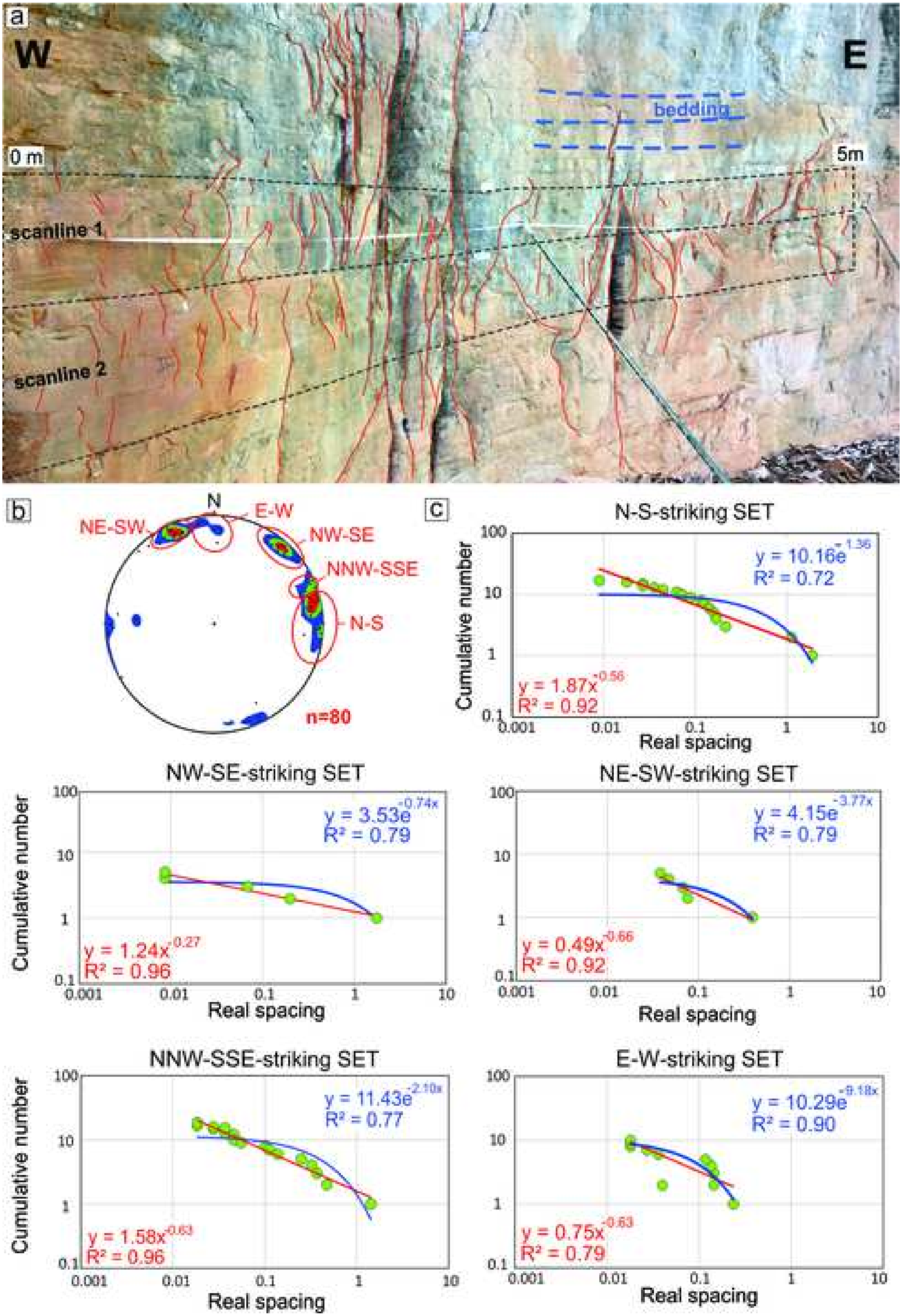

Figure 13

Click here to access/download;Figure;13 Lapinha.jpg

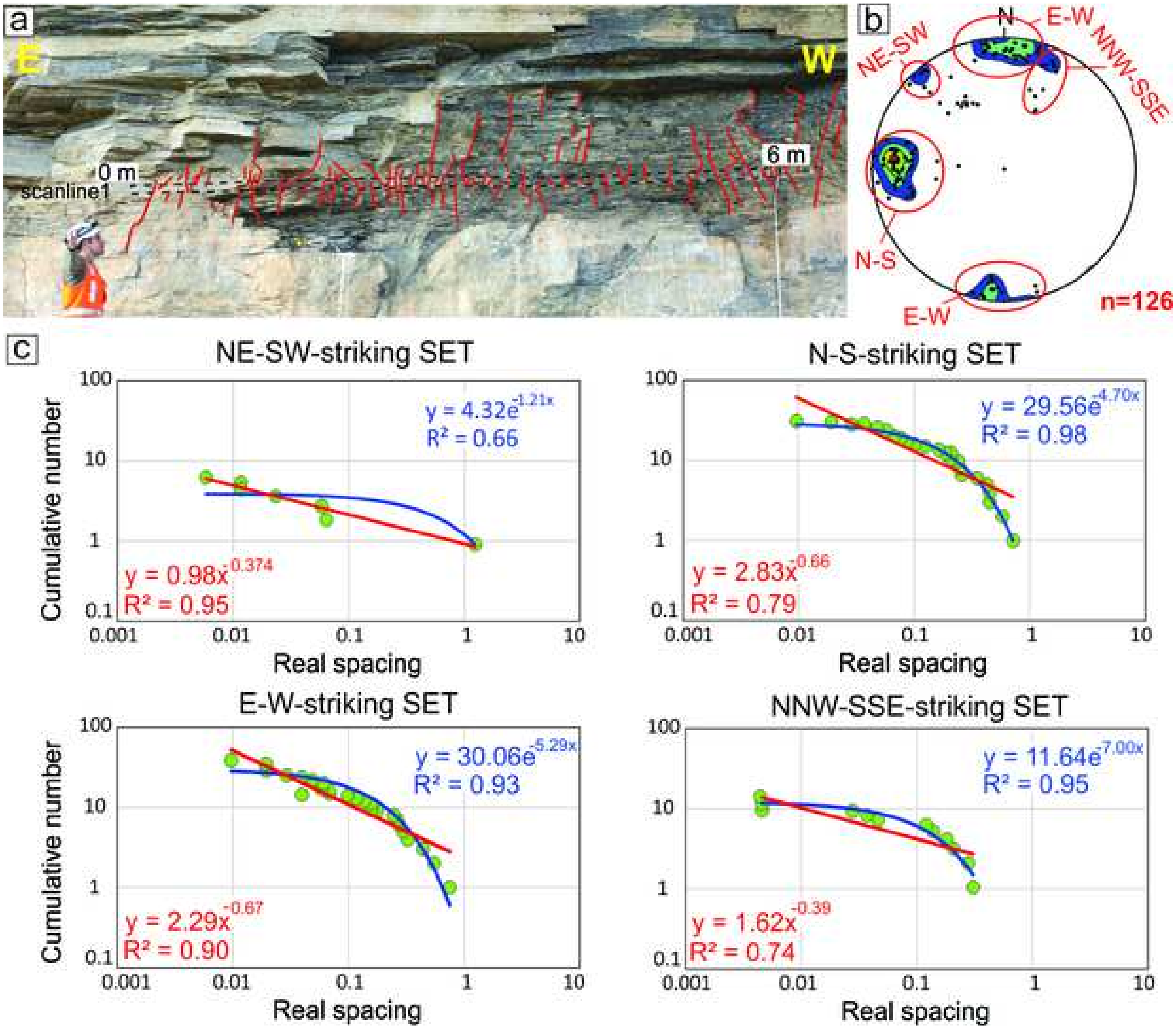

Figure 14

Click here to access/download;Figure;14 torrinha.jpg

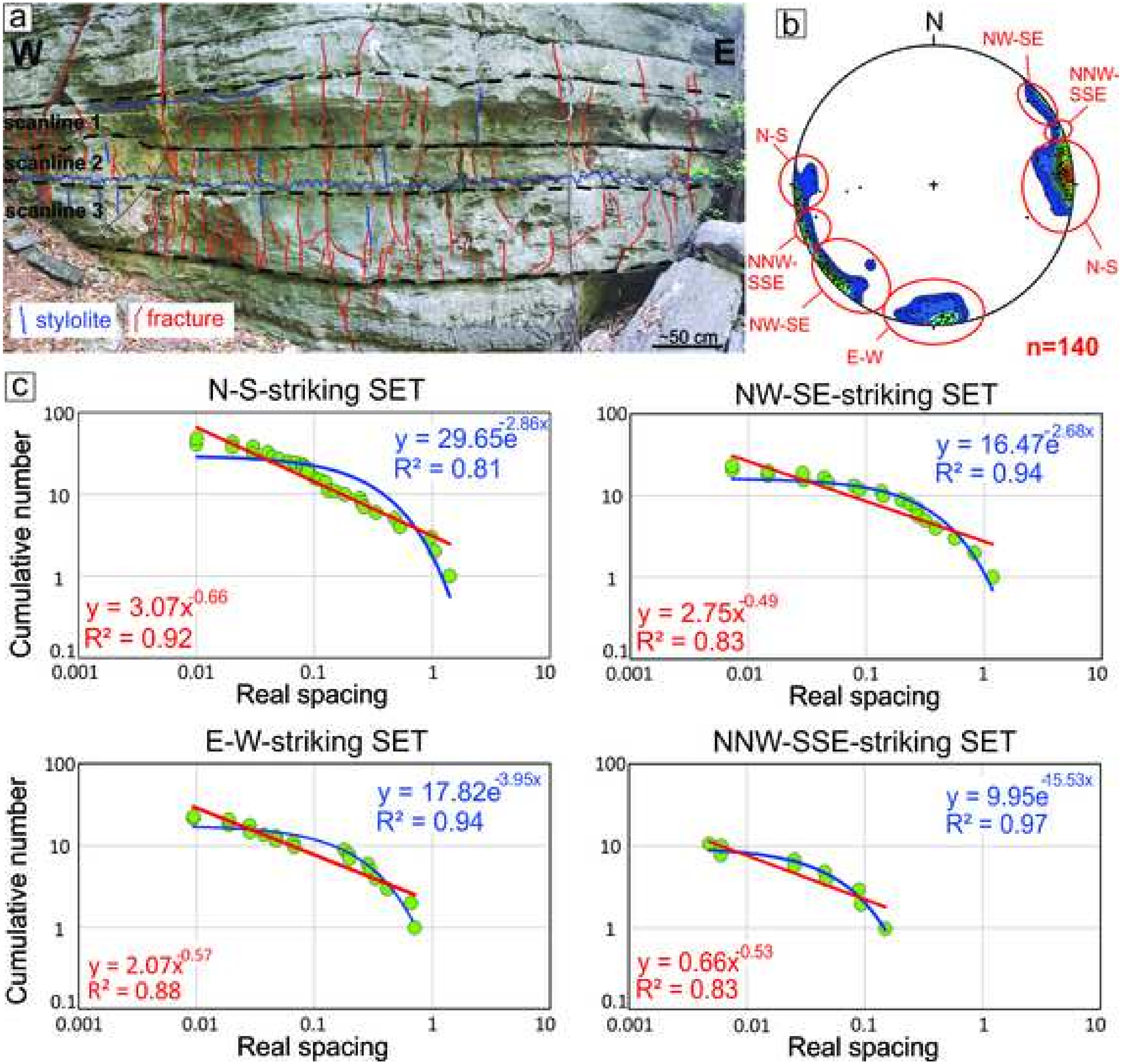

Figure 15

Click here to access/download;Figure;15 paixao scanline.jpg

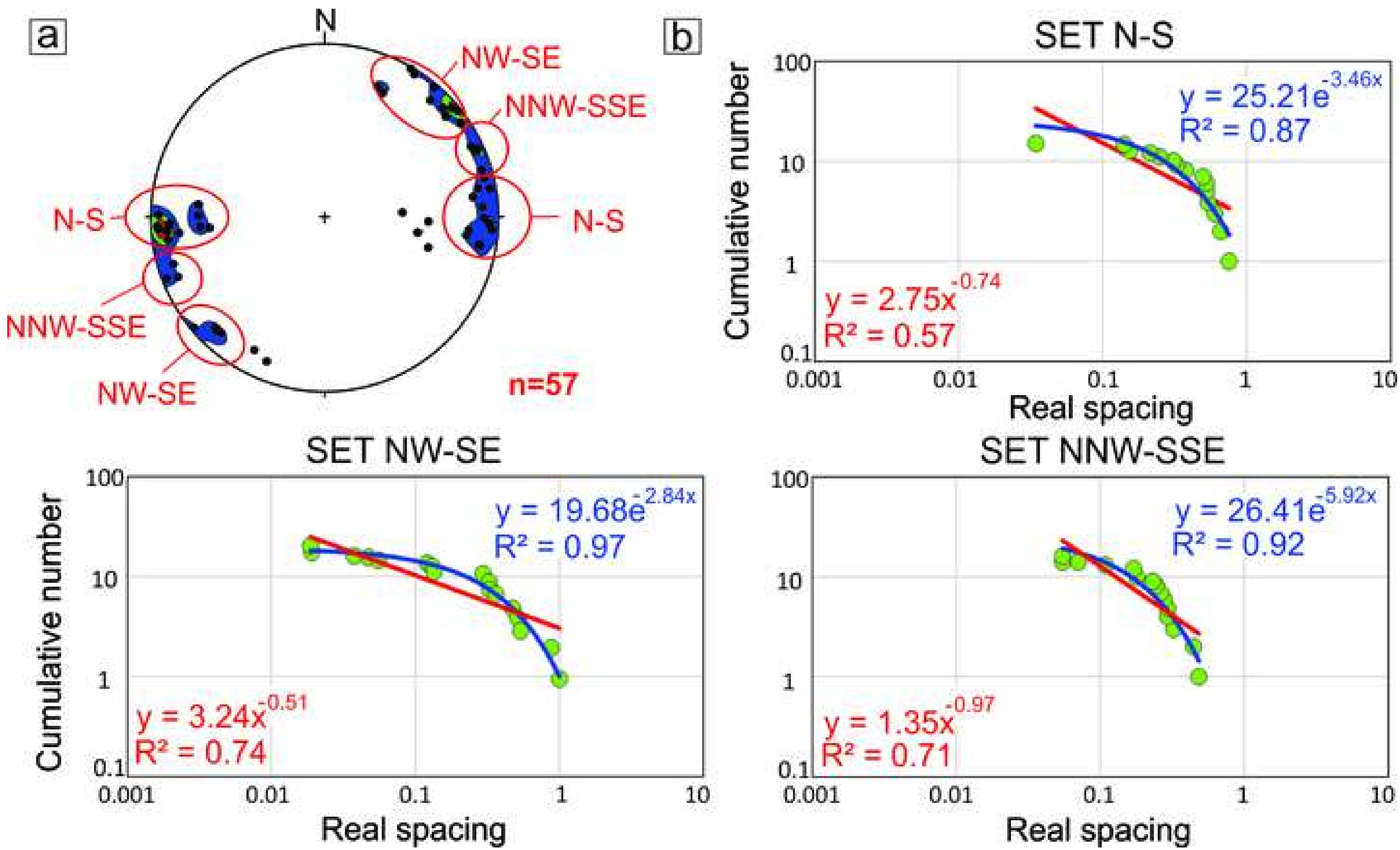

Figure 16

Click here to access/download;Figure;16 modelo falha conclusion.jpg

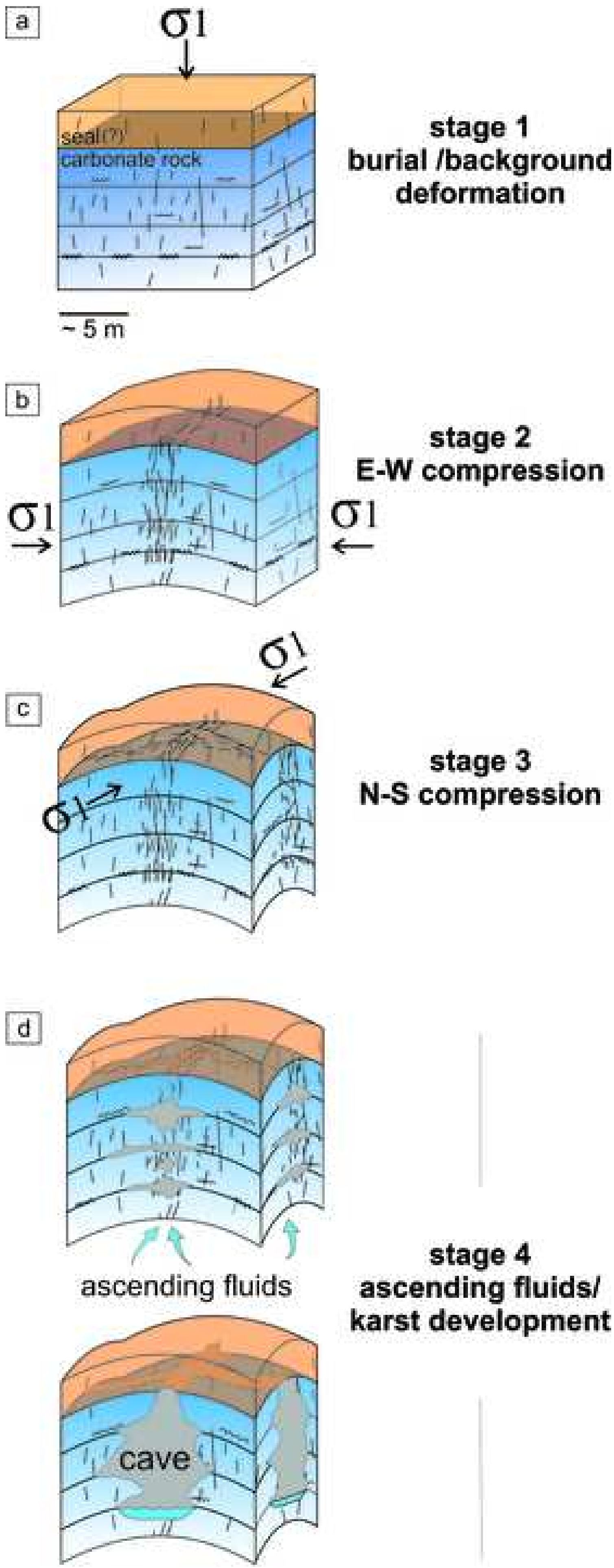

Table 1

Click here to access/download
Table
Table 1.docx

Declaration of interests

☒ The authors declare that they have no known competing financial interests or personal relationships that could have appeared to influence the work reported in this paper.

☐The authors declare the following financial interests/personal relationships which may be considered as potential competing interests: